Dissertation

submitted to the
Combined Faculties for the Natural Sciences and for Mathematics
of the Ruperto-Carola University of Heidelberg, Germany
for the degree of
Doctor of Natural Sciences

presented by
Diplom-Physiker Jörg Rottmann
born in Hannover, Germany

Oral Examination: July 25, 2012

Non-invasive lung tumor motion estimation and mitigation in real-time during radiation therapy

Referees: Prof. Dr. Uwe Oelfke
                              Prof. Dr. Ross Berbeco

Abstract

Intrafractional lung tumor motion during the application of external beam radiation therapy can be a limiting factor for the treatment outcome. Tumor motion can cause marginal underdosage of the target volume as well as severe radiation toxicity in the surrounding healthy tissue. This thesis consists of three parts: The first part presents a novel method for real-time lung tumor motion estimation that does not require the surgical implantation of fiducial markers. The method utilizes fluoroscopic megavoltage x-ray images acquired with the therapy beam throughout the treatment delivery and does therefore not require to expose the patients to additional imaging dose. The algorithm is validated by retrospective analysis of images acquired during irradiation of a dynamic chest phantom as well as images acquired during lung SBRT treatment deliveries to patients. The root mean square geometric error was found to be $< 1\,\mathrm{mm}$ for phantom data and $(2.1 \pm 1.7)\,\mathrm{mm}$ for patient data, respectively. The second part of this thesis describes an integrated system capable of moving the treatment aperture in synchrony with a moving treatment target to mitigate tumor motion during radiotherapy. The system utilizes a dynamic multi-leaf collimator tracking system to drive the treatment aperture in real-time and a special frame grabber to allow for fast image acquisition. A linear prediction algorithm was implemented to overcome the system latency ($\approx 250\,ms$). The measured root mean square geometric error was reduced from 2.4 - 3.5 mm to $< 1\,\mathrm{mm}$. In the third part of this thesis, a concept utilizing the tumor motion estimation algorithm to calculate delivered dose is presented. The concept is validated with a dynamic chest phantom and applied in retrospect to imagery acquired during a lung SBRT treatment. It is shown that marginal underdosage can be quantified with a dose volume histogram (DVH) calculated from the analyzed data.

Zusammenfassung

Die interfraktionelle Bewegung von Lungentumoren während der Applikation von externer Strahlentherapie kann ein limitierender Faktor für den Behandlungserfolg sein. Tumorbewegung kann sowohl eine Unterdosierung des Zielvolumens als auch eine schwerwiegende Überdosierung des umliegenden gesunden Gewebes zur Folge haben. Die vorliegende Arbeit besteht aus drei Teilen. Im ersten Teil wird eine Methode zur bildgestützten Bewegungsabschätzung von Lungentumoren in Echtzeit vorgestellt. Vorteile des Verfahrens sind die Unabhängigkeit von implantierten Markern (Pneumothorax Risiko) und die Vermeidung von zusätzlicher Bildgebungsstahlendosis, da das Verfahren mit dem Therapiestrahl akquirierte fluoroskopische Bildsequenzen nutzt. Die Validierung erfolgte sowohl anhand von Bildern, die mit einem beweglichen Thoraxphantom aufgenommen wurden, als auch anhand von Bildern, die während einer Reihe von Lungenstereotaxiebehandlungen aufgenommen wurden. Der Fehler (rmse) wurde für den Phantomdatensatz zu $< 1\,\mathrm{mm}$ und für den klinischen Datensatz zu $(2.1 \pm 1.7)\,\mathrm{mm}$ bestimmt. Der zweite Teil dieser Arbeit befasst sich mit der Implementierung und Charakterisierung eines dynamischen, adaptiven Bestralungsystems, das durch das Nachführen des Therapiestrahls in Echtzeit Bewegungen des Zielvolumens kompensieren kann. Das System nutzt eine computergestützte, dynamisch ansteuerbare Strahlungsapertur (MLC), welche mit der Position des Zielvolumens aus dem ersten Teil in Echtzeit angesteuert wird. Die Latenzzeit wurde gemessen ($\approx 250\,ms$) und durch einen linearen Vorhersagealgorithmus kompensiert. Das System wurde mit einem mit Lungentumortrajektorien programmierten dynamischen Thoraxphantom getestet. Der Fehler konnte von $2.4\,\mathrm{mm}$ bis $3.5\,\mathrm{mm}$ auf unter $1\,\mathrm{mm}$ reduziert werden. Im dritten Teil dieser Arbeit wird der Algorithmus vom ersten Teil eingesetzt, um nach jeder Fraktion einer Lungenstereotaxiebehandlung die applizierte Dosis zu berechnen. Das Konzept wurde mit einem dynamischen Thoraxphantom validiert. Mit der retrospektiven Bildanalyse einer Lungenstereotaxiebehandlung konnte gezeigt werden, daß sich fraktionelle Unterdosierungen des Zielvolumens, etwa durch nicht optimale Patientenpositionierung, mit dieser Methode in Form eines Dosis-Volumen Histogramms (DVH) quantifizieren lassen.

Contents

List of Figures

1 Introduction

In this chapter a brief overview of the context of this thesis is given. In Section 1.1 the focus of this work on external beam lung cancer radiotherapy is motivated. An introduction to the most relevant aspects of radiotherapy is given in Section 1.2 leading to stereotactic body radiation therapy which is discussed in Section 1.3. The core problem addressed in this thesis, (intrafractional) tumor motion, is found in Section 1.4. Finally in Section 1.6 a brief overview of the topics covered in this thesis is given and the publications extracted from this manuscript are disclosed.

1.1 Motivation

The American Cancer Society estimated for 2011 that over 570,000 people in the US died from cancer, making it the second leading cause of death (after cardiovascular diseases). Men are contributing with about 300,000 fatal cases, slightly more than women with about 270,000 cases ACS [1]. Lung cancer is among the types of cancer with the worst survival rates. The average five-year relative survival rate was estimated to 15.8% for the years of 1999-2006 in the United States and 13.2% in Germany[1].

For well defined tumor volumes, radiation therapy is one of the major treatment choices. While it may be used as the sole treatment option, it is more commonly used in combination with chemotherapy and/or surgical removal of malignancies.

1.2 External beam radiotherapy basics

The goal of external beam radiation therapy is to limit or reduce the proliferation of malignant/cancerous cells by delivering a sufficient dose of ionizing radiation

---

[1]While these percentages demonstrate the generally low survival rate, they can not be directly quantitatively compared as the data are collected in different studies and may therefore also reflect different criteria of detection, data quality and treatment availability
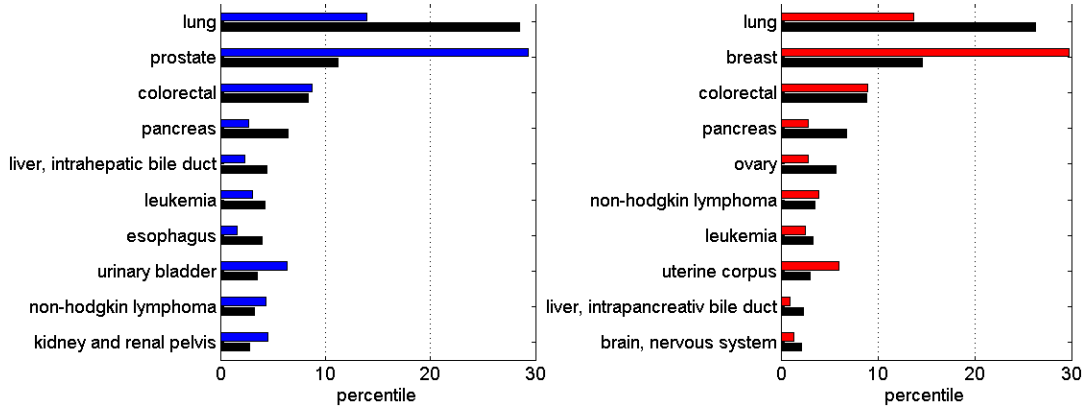
Figure 1.1: Estimated cancer death rates in the United States for the 10 most common disease sites (data extracted from ACS [1]). The number of total cancer caused deaths in the US in 2011 is estimated to be 300,430 men and 271,520 women including a total of 85600 men and 71340 women for lung cancer alone. That makes lung cancer the largest contributor to cancer related deaths in 2011 in the US. The 10 most common disease sites are shown above in *(red)* for women and in *(blue)* for men.

to cause substantial cell death in the irradiated tissue volume. Radiation types used clinically for this purpose include photons, electrons, hadronic ions such as protons or carbon and sometimes neutrons. Treatments with high energy photon beams account for the majority of clinical cases because they are much easier (cheaper) to generate and handle than any of the heavy particles. High energy photon beams can be generated with a linear accelerator (LINAC) in which electrons are accelerated, resulting in a roughly monoenergetic electron beam. Typical electron energies clinically used are in the range of 4-18 MeV. The beam is sent through a target material with high atomic number (e.g. a tungsten alloy) producing a continuous spectrum of Bremsstrahlung with an average energy of roughly 1/3 of the incident nominal electron energy[2]. This thesis focuses only on radiation therapy with high energy photon beams. Therefore all references are to be seen in this context unless otherwise explicitly stated.

There are several different techniques to deliver a planned photon fluence to a patient. However, they all share a similar workflow from diagnosis to treatment

---

[2]The photon beams are labeled by their respective maximal energy, i.e. the energy of the generating electrons. The unit MV is used in stead of MeV (as for particles) to distinguish this fact.
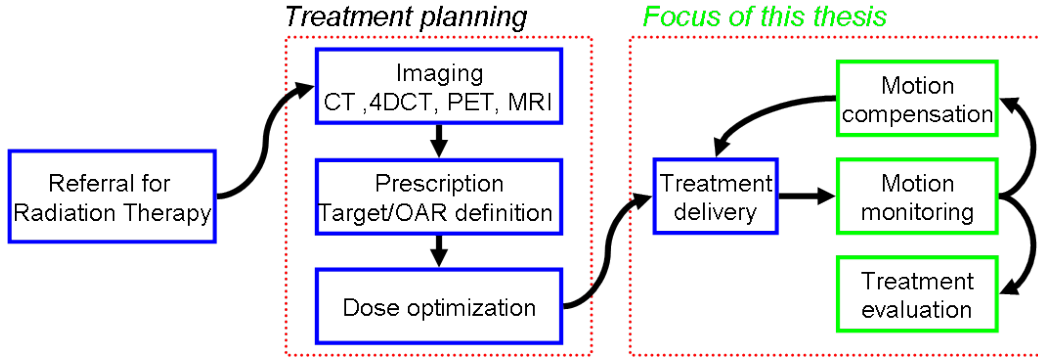
Figure 1.2: Workflow of a typical radiotherapy treatment from diagnosis to treatment delivery. The *green* boxes correspond to Chapter 2, Chapter 3, Chapter 4 which contain the authors research contribution in this thesis.

delivery. A flowchart of this process is depicted in Figure 1.2. In the following sections a brief overview of the steps involved is given.

1.2.1 Treatment planning

Prior to the initiation of radiation therapy, volumetric images are acquired. Usually this includes at least a conventional 3D computed tomography (CT) to get the anatomy and electron density distribution of the patient, but depending on the case this can also include magnetic resonance imaging (MRI) or positron emission tomography (PET) to help distinguishing malignancies from healthy tissue. To be able to compare anatomical structures between these imaging modalities, they are transformed into a common coordinate system by image registration techniques.

The volume to be irradiated as well as the volumes to be spared are contoured on the CT in conjunction with the other imaging modalities (where necessary). The physician's prescription defines dose constrains to these volumes. The most important structures used for this purpose are defined in the ICRU reports 50 and 62 [24, 25]. They are illustrated in Figure 1.3 on the right side[3]:

- **GTV** The *gross tumor volume* encloses all visible parts (from the radiologic images) of the malignancy and is considered the volume of known tumor infiltration.

---

[3]The volumes depicted are reflecting the definitions actually used for treatment planning at the institution this research was conducted - there is therefore a difference to the ICRU report definition.

- **CTV** The *clinical target volume* encloses the suspected[4] tumor infiltration surrounding the GTV. This is also referred to as the microscopic disease.
  It has been disputed whether inclusion of suspected microscopic disease with an additional margin actually improves tumor control and how large this margin should be (since only a pathologic examination can reliably distinguish the penetration depth of tumor cells). For lung tumors a pathologic examination however would bear the risk of pneumothorax.

- **ITV** The *internal target volume* encloses all positions of the GTV that are expected to occur due to organ motion. This concept will be discussed in more detail in Section 1.4.

- **PTV** The *planning target volume* encloses all the previous volumes and adds an additional fixed margin around them to account for any kind of patient position inaccuracies on the treatment table and inaccuracies expected from the beam alignment. The goal is to ensure that the prescribed dose to the CTV can be actually delivered with a certain probability.

- **OAR** *Organs at risk* are critical normal anatomical structures that are particular sensitive to radiation and need to stay under a certain dose threshold. For lung cancer this often includes the lung tissue, heart, spine, esophagus and chest wall.

It should be noted that the definition of these volumes is operator dependent. In two studies conducted by Van de Steene et al. [69] and Giraud et al. [20] significant inter-observer variability in GTV delineation of lung tumors was found.
In the next step a treatment planning system (TPS) is utilized to define a beam configuration and optimize photon fluence maps for each of these beams, so that the superposition of all beams creates a dose distribution within the patient that meets the constraints of the prescription to the PTV and OARs.

1.2.2 Treatment delivery with gantry and MLC

There are several types of treatment machines that incorporate a LINAC. This thesis focuses only on the type that features a room-fixed linear accelerator and a gantry rotating around a couch table to deliver a photon (or elecctron) fluence from various incident angles shaped by a computer controlled beam aperture, a

---

[4]This margin is not assigned on basis of radiologic evidence but as a fixed margin.
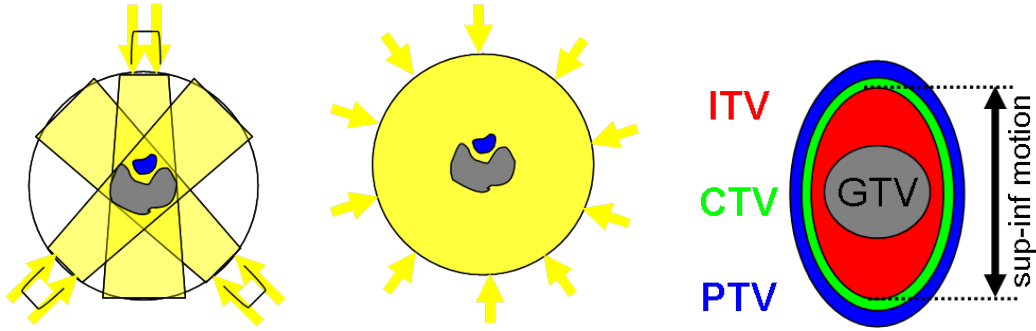
Figure 1.3: Common radiotherapy delivery techniques: on the *(left)* a setup for 3D conformal radiotherapy is shown. The gray area is the tumor, the blue an OAR. Each beam has a flat fluence profile. IMRT may have the same beam arrangement, but the fluence profile would be shaped non-flat to spare the (blue) OAR while keeping the dose to the target conformal. Rotational therapy *middle* delivers a shaped fluence profile while rotating in an arc around the patient. The total volume of irradiated tissue is larger, but the dose constraints can be met at least as well as with IMRT if not better. On the *(right)*, the various treatment planning margins are illustrated.

multi-leaf collimator (MLC).

There are three prominent techniques to deliver a high energy photon beam with such as treatment machine that have been developed over time and feature increasing complexity. They are illustrated in Figure 1.3 for comparison.

1. *3D conformal* is the simplest of the modern techniques for radiotherapy delivery. A number of incident photon beam angles are defined by the treatment planner. The superposition of these beams creates a high dose volume in the PTV while the entry and exit paths of the individual beams imposes only moderate dose to the surrounding normal tissue (see *(left)* of Figure 1.3). The shape as well as the photon fluence intensity are optimized by the treatment planner.

2. *Intensity modulated radiotherapy* (IMRT) allows the fluence maps for each beam to be non-uniformly shaped. This can be achieved by dynamically adjusting the beam aperture with a multi-leaf collimator and thus to "paint" a fluence map. This additional degree of freedom to the incident fluence allows steeper dose gradients and more conformal dose distributions. The fluence maps are calculated in the TPS by an algorithm iteratively optimizing a simulated dose distribution in the patient to meet the dose constraints to the PTV

and OARs.

3. *Rotational therapy* is a recently introduced delivery technique. It is similar to IMRT, but the beam stays on while the gantry is rotating around the patient and the dose rate (beam intensity) as well as the beam aperture are modulated. This creates a delivery with more degrees of freedom to shape individual dose distributions (see *(middle)* of Figure 1.3). A desirable feature of this technique is shorter treatment time while allowing similar complexity for the dose distribution as IMRT. A concern may be the larger volume of normal tissue irradiated (in comparison to 3D conformal and regular IMRT).

1.3   Stereotactic body radiation therapy for lung cancer

Stereotactic body radiation therapy (SBRT) is a type of radiation therapy that has in recent years become a very popular treatment option for small, well localized lung tumors. To distinguish stereotactic body radiation therapy from conventional radiotherapy, a summary of the most important differences and their respective implications will be given in the following:

Conventional lung cancer radiation treatment

The prescribed dose is divided into about 20-30 "fractions", i.e. the patient receives 20-30 daily treatments. Another option sometimes used to treat a minority of lung cancers is *"bis in die"* (BID) fractionation, where treatments are given twice daily separated by at least 6 hours. The rationale behind this practice comes from radiobiology and is twofold:

(i) The time between fractions allows the repair of sublethal cell damage in normal tissue and therefore decreases the toxicity induced by the treatment in those cells. This is particularly important with respect to the OARs.

(ii) Radiation sensitivity is not equal in all of the phases of the mammal cell cycle. Fractionation allows the cell cycles of the cancerous cells to redistribute and thus increases the number of cancerous cells in a more radiosensitive phase.

Stereotactic body radiation therapy (SBRT)

The treatment course for SBRT consists of only a few fractions (typically 3-5) with a significantly higher dose per fraction. While the total dose administered over the treatment course is similar to a conventional treatment course, the biological equivalent dose is higher resulting in more aggressive malignant cell kill. The concept of fewer but higher dose fractions is called hypofractionation and has been successfully applied in intra-cranial treatments for decades. However, a major concern with hypofractionated treatment types are the potentially high doses to the surrounding normal (lung) tissue which can cause serious side effects such as radiation pneumonitis[5] and can even become potentially fatal. Therefore treatment margins are reduced and dose gradients are increased to keep the dose distribution tightly bound within the PTV. However, this approach puts additional importance on a precise patient setup on the treatment table, i.e. the alignment of the patient's anatomy to match the planning position defined in the planning CT. While achieving high setup accuracies with cranial fixations is comparatively easy to achieve[6] it is more challenging to set up to organs that do not have such a well defined position within the human body (such as lung, liver, etc.). Therefore it has only been in recent years with the emerging availability of image guidance in the treatment room that hypofractionated treatments have become sufficiently safe to be also applied for extra-cranial tumor locations. With the first treatment outcome studies published in 1995 [8], it became evident that SBRT could be a promising treatment option also for extra-cranial sites. Studies in Germany conducted on treating cancers of the liver [22] and lung [72] as well as studies in the United States on early stage lung tumors [67] indicated good SBRT treatment outcomes for small and well localized lesions in the thoracic and abdomino-pelvic cavity. An extensive review of the current state of the art in SBRT as well as a comparison to conventional IMRT and 3D conformal treatments can be found in Benedict et al. [5] and the references therein.

At first the main rationale for the use of lung SBRT was to establish an alternative to surgical resection for normally inoperable patients (many lung cancer patients are elderly and/or have other complicating health conditions). The promising outcome studies have established this technique as a viable alternative treatment

---

[5]Pneumonitis = infection of the lung tissue

[6]The underlying assumption is that the brain is in a fixed relationship with respect to the cranium.

option to surgical resection for small, early stage lung tumors[7]. Grills et al. [21] consider SBRT for lung tumors even as the favorable treatment option to surgical resection showing only minimally adverse effects.

1.4   Tumor motion during radiotherapy

Tumor motion is of great concern for the accurate delivery of radiation therapy as it affects both tumor coverage and normal tissue toxicity. While reduced coverage can compromise the treatment outcome, normal tissue toxicity can be particularly problematic if there are organs at risk (OAR) located immediately adjacent to the target volume (PTV). In the context of lung tumor treatment it is important to note that lung tissue itself is considered an OAR.
Tumor motion may be divided into two categories:

→ **interfractional motion** denotes changes in the mean tumor location as well as deformations of the tumor volume in between treatment days. The setup errors made when the patient's anatomy is aligned to the planning CT on the treatment table is an example for an interfractional change in tumor position. The shrinkage of the target volume over the therapy course is an example of deformation.

→ **intrafractional motion** describes changes in tumor location and shape that occur during the delivery of the treatment. Intrafractional motion due to respiration can be substantial for thoracic and abdominal tumor sites. The analysis of lung tumor motion range has been the objective of several publications and it was observed that superior-inferior motion amplitudes can be in the centimeter range (Ekberg et al. [15], Chen et al. [11], Seppenwoolde et al. [60]).

While interfractional motion causes a rigid shift of the delivered dose distribution, intra-fraction motion causes the dose distribution to average out (blurr). Both effects cause a deviation between planned and delivered dose.
Conventional radiotherapy tends to be less sensitive to interfractional motion than SBRT treatments due to the relatively large number of fractions that tend to average out errors (if one assumes that the setup errors are distributed at

---

[7]Stage I/IIa - meaning that the tumor has not metastasized and has a relatively small volume.

random over the course of the treatment).

While the interfractional motion may be reduced by more thorough patient setup, the intrafractional motion is harder to account for. Particularly for lung SBRT with its sharp dose gradients and high doses per fraction, tumor motion can become prohibitive for treatment. Therefore intrafractional tumor motion is dealt with from several perspectives that will be briefly described in the following sections.

1.4.1 Accounting for motion in treatment planning

Tumor motion is often accounted for in the treatment plan by an expansion of the volume planned to receive the full prescription dose level. The rationale behind this strategy is that a sufficiently sized irradiated volume will contain the tumor at all times during the treatment delivery, even in the presence of interfractional and intrafractional motion and therefore provide full dose coverage to the tumor.

The ITV is the volume intended to mitigate intrafractional tumor motion. It is derived from the motion range and pattern observed on volumetric images like CT or 4DCT which are used for treatment planning. The PTV is a patient independent fixed margin expansion to the ITV and is intended to mitigate the effect of interfractional motion on the target dose coverage. However, it has been shown that motion range and pattern of the tumor may vary from day to day (interfractionally) as well as during treatment delivery (intrafractionally) (Seppenwoolde et al. [60]). For lung SBRT the escalated doses per fraction in combination with the reduced margins constitute an increased risk of a marginal miss[8] which can occur even from just one fraction.

A 4DCT depicts the temporal changes in a patient's anatomy during respiration. It consists of a number of CT volumes (usually 10) each resembling a different phase of the patient's breathing cycle. So, a simple technique to define an ITV from a 4DCT is to contour the union of all the breathing phases. However, a large ITV can mean excessive irradiation of normal tissues. As mentioned already in Section 1.3, radiation toxicity to normal tissue can impose serious problems such as radiation pneumonitis. Therefore, the total dose must often be lowered in order to limit normal tissue toxicity, compromising therapeutic efficacy of the

---

[8]A *marginal miss* means that the tumor volume is partially (i.e. on its margin) not covered within the treatment aperture and thus (for the treatment outcome) significantly underdosed.

Figure 1.4: Patient in a compression plate. The stamp compresses the patient's abdomen which usually reduces the motion range of the internal organs. The level of motion reduction is strongly patient dependent..

treatment.

Adaptive radiotherapy

A different approach is followed in *adaptive radiotherapy* (Yan et al. [74], Sonke and Belderbos [64]). Here, the idea is to monitor the treatment delivery and calculate from the observed motion a dose estimate for already delivered treatment fractions. The already delivered dose fraction can be utilized to calculate an updated optimized treatment plan for the delivery of the remaining fractions and mitigate the potential for a compromised target dose in this way.

1.4.2   Strategies to reduce or compensate motion

Several methods have been proposed to control tumor motion during radiotherapy. They may be divided into passive and active techniques:

Passive control is geared towards reducing the (residual) motion range.

→ A device frequently used in clinical operation is the ***compression plate***. The patient's abdomen is compressed by a stamp (the compression plate), limiting internal organ motion. However, Murray et al. [44] and Kontrisova et al. [34] state that the devices motion limiting capabilities are patient dependent. Also, many patients find the procedure intolerable (breathing discomfort, pain).

Figure 1.4 shows a person on the treatment table with a compression plate in place. Additionally it should be noted that planning CT images are acquired with the device in place, limiting the visible motion. The residual motion range on the treatment table therefore may not be the same as the one observed during the imaging session.

→ Another approach to reducing residual tumor motion during beam-on time is the ***breath hold technique***. The patient is asked to hold the breath while the beam is on. Several groups have investigated various implementations. Most prominent is a combination with a spirometer that measures the current lung volume to define a reproducible breathing phase. However, particularly for lung patients with already reduced lung functionality it can be very discomforting to hold one's breath even for 10-20s.

Active control methods are not seeking to limit the target motion but rather to compensate for it by adapting the treatment delivery. Therefore knowledge of the tumor location throughout the treatment needs to be available. How to gather this information will be discussed in the next chapter.

→ For ***respiratory gating*** the treatment beam is only switched on while the tumor is within a pre-defined position window, thus confining the motion range impacting the treatment delivery. If the tumor moves out of this window, the treatment beam is switched off and the system waits until the tumor returns to the window. Internal markers (Shirato et al. [62]) as well as external surrogates (Berbeco et al. [7]) have been used to trigger the beam switching.
The advantage of this technique is that even patients that show a large tumor range despite passive control methods can be treated. However, disadvantages include the increased duration of the treatment delivery as well as the limited reliability of the commercial implementations.

→ During ***dynamic beam tracking***, the tumor is followed with the radiation beam with the help of a multi-leaf collimator (MLC) (Keall et al. [30]), while ***dynamic couch tracking*** moves the couch to keep the tumor within the treatment aperture (D'Souza et al. [14]). The goal for both of these techniques is to keep the target volume "frozen" within the treatment aperture despite its motion. To accomplish this, both techniques require two components: (i) real-time knowledge of the target position and (ii) the ability to

adapt the aperture (or couch) position in real-time accordingly.

Both components will be discussed in detail in Chapter 2 and Chapter 3, respectively.

$\rightarrow$ Cyberknife$^{\circledR}$ is an alternative radiotherapy delivery technique that is capable of active motion compensation. Unlike the conventional room-fixed LINAC, steering the electron beam with bending magnets through a gantry of only one rotational degree of freedom, the Cyberknife$^{\circledR}$ approach features a small LINAC mounted on a robotic arm, allowing virtually any radiation beam incident angle[9]. Active motion management is available with a built-in system using external markers as well orthogonal x-ray tubes to update the motion correlation model between external and internal positions signal. However, due to the "dose painting" with a small diameter radiation beam an average treatment delivery takes about two hours which is about 3-6 times as long as a linac-based lung SBRT fraction.

For the active methods of tumor motion control robust real-time tumor localization is needed. This will be the topic of Chapter 2.

1.5   Image guidance in the treatment room

The aforementioned implications of tumor motion have driven an increased demand for improved patient setup and motion monitoring capabilities in the treatment-room. Most radiation therapy machines in clinical use at the moment feature two devices that allow in-room image acquisition: an *on board imager* (OBI) and an *electronic portal imaging device* (EPID). Both can potentially be used during treatment delivery. In the following sections a brief description of both of these tools is given, however the EPID is discussed in greater detail because this thesis is based exclusively on the use of this device.

1.5.1   The on-board imager

The *on board imager* (OBI) is a diagnostic kilovoltage (kV) x-ray tube mounted on the gantry. Most commercially available systems have the OBI's beam line at an

---

[9]For safety reasons this is actually limited to a pre-defined grid of positions. In this way potential collisions from an errornous position request can be avoided.
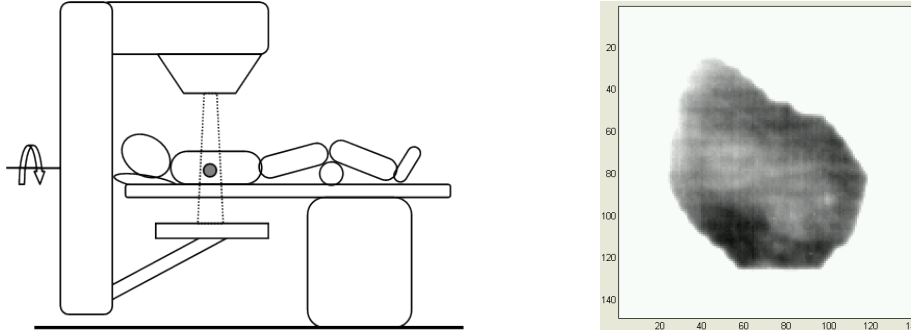
Figure 1.5: *(left)* Illustration of a typical radiotherapy setup on a LINAC with a gantry. The radiation beam leaves the collimator, passes through the patient and is captured by the EPID. The arrow denotes the axis of rotation for the gantry. *(right)* EPID image showing a patient's lung tumor during SBRT delivery. Only digital enhancement applied is a window/leveling to maximize the display contrast within the treatment aperture.

angle of 90° with the therapeutic beam line[10]. The OBI allows the capture of high quality radiographs as well as fluoroscopy and cone-beam computer tomography (CBCT). While it is generally possible to use the OBI during therapeutic beam-on time, a degradation in image quality is observed from additional scatter.

1.5.2   The electronic portal imaging device

The electronic portal imaging device (EPID) captures the exit fluence of the therapy x-ray beam after passing through the patient (see Figure 1.5 for a sketch). Images acquired with this detector depict the patient's anatomy in the therapy beams-eye-view perspective making them an excellent tool for the verification of the patient setup in the treatment room (with respect to treatment planning). The research presented in this thesis is based on images acquired with such a device. Therefore a brief introduction to its history, detector physics, limitations and current state of technology as well as clinical use is given in the following section. Relevant specifications of the EPID used in this thesis are summarized at the end of the section.

---

[10]As an exception to this the Siemens Artiste® has an OBI featuring an imaging beam line parallel to the therapeutic beam line. However, this product has been discontinued as of early 2012.

History of portal imaging

Before the introduction of electronic devices for megavoltage imaging, predominantly film cassettes were used to acquire port images in radiotherapy. A film cassette consists of a metallic front plate (typically $\approx 1\,mm$ copper), a sheet of radiographic film and a backplate usually made of plastic. Between front plate and film sometimes a phosphorous material is used. The metal front plate serves a dual purpose: it filters out the scattered electrons from the patient/couch which would otherwise greatly reduce the image quality (provided of course that the thickness of the plate is larger than the incident electron range in that material). The other purpose is to serve as a build up region for the generation of secondary electrons that can then interact with the image receptor (e.g. film). The function of the back plate is to reduce backscatter which can also significantly reduce the image quality (film interactions with backscattered electrons add no radiologic information but blacken the film, potentially saturating it).

There were several disadvantages connected with film, the most important one being the time needed to develop the film which even with fast methods is in the range of minutes. Therefore portal films were usually not taken for every fraction but rather once a week or even less. This triggered the quest for alternative technologies allowing for immediate display of the port image. Having images in electronic form gives also the opportunity to enhance these images by image processing algorithms, the simplest being the adjustment of the window/level[11].

The first generation of commercialized EPID devices was available for clinical operation in the late 1980s. These devices used a phosphorous screen that converted the electrons generated in the front plate into visible light which then was recorded by a camera. To accomodate with the limited space requirements as well as to protect the camera electronics from the therapy beam, the camera was not directly mounted under the phosphor screen but was focused on it via a mirror reflecting the image.

The second generation of commercially available EPIDs entered clinical usage in the year of 2000 and continues to be a widely applied technology in the year of 2012. The phosphorous screen in these devices was replaced by a scintillator[12]

---

[11]The window/leveling operation constraints the mapping of the image gray values to the display gray values by selection of an image gray value range. This enhances therefore display contrast for the selected gray value range.

[12]See Nikl [46] for a comprehensive review for x-ray scintillators (and phosphors).

Figure 1.6: Illustration (not to scale) of the most important layers of an active matrix flat panel imager (AMFPI) such as the AS-1000. The front plate is typically $\approx 1\,mm$ copper. It can shield from scatter electrons and converts the incident megavoltage photons to secondary electrons that can then interact with the scintillator. The photodiode converts the light generated in the scintillator to electric charge. The thin film transistor (TFT) serves as a switch to read out the collected charge.

and the camera has been replaced by an *active matrix flat panel imager* (AMFPI) which is placed directly under the scintillator material. The AMFPI is a matrix detector in which each pixel consists of a (discrete) hydrogen doped amorphous silicon (a-Si:H) photodiode and a thin film transistor (TFT) as a switch to allow readout. A simplified drawing of a pixel is shown in Figure 1.6 along with the specifications of the EPID used in this thesis.

Image quality

The quality of MV portal images is unfavorable when compared to diagnostic x-ray images. This is mainly due to the higher energy of the photon source[13]. In addition, the relatively large source size of the radiation beam can cause blurring on the images.

In the following, the main reasons for the poor image quality are discussed in the context of some quantitative measures that are commonly used for the evaluation of "image quality":

→ *Signal to noise ratio (SNR)* For medical images it has been suggested (Motz and Danos [42]) that a signal cannot be properly distinguished from the underlying noise if SNR < 5. There are several main contributions to the noise level in an EPID one may expect: photon shot noise, noise from scattered photons (due to objects in the beamline) and (electronic) noise from

---

[13]Diagnostic images are typically acquired at energies in the range of $< 150 kVp$, while the therapy beam has an energy of typically $\geq 6 MV$.

the detector itself. Neglecting the detector noise the SNR can be written as(Herman et al. [23]):

$$\text{SNR} := \frac{signal}{noise} = \frac{signal}{\sqrt{\text{mean}(signal)}} = \frac{\Phi_2 - \Phi_1}{\sqrt{0.5 \cdot (\Phi_1 + \Phi_2 + 2\Phi_S)}} \qquad (1.1)$$

Here Φ_1, Φ_2 denote the primary fluences reaching the detector after traversing anatomical structures 1 and 2, respectively and Φ_S denotes the scattered fluence. Therefore the SNR improves with increasing incident photon fluence. However, Herman et al. [23] point out that "it appears that poor image quality is not because the image receptors do not have enough x-ray quanta interacting in them, but because the image receptors either add additional noise to the images or display the images so that noise in the eye-brain system becomes important".

$\rightarrow$ *Quantum efficiency* measures the fraction of incident photons creating a signal in the detector. However, a more descriptive definition for detectability of an object is the *detective quantum efficiency (DQE)* given by the ratio of the incident to the output SNR. Currently commercially available EPIDs (including the as1000 from Varian Medical Systems used in this thesis) have a quantum efficiency of $< 5\%$ and a DQE $\leq 1\%$ (Antonuk [2]).

$\rightarrow$ *Subject contrast* quantifies how distinguishable two objects are from each other on a given image. Following the definition of Motz and Danos [42] the portal image contrast C may be written as:

$$C := \frac{signal}{\text{mean}(signal)} = \frac{\Phi_2 - \Phi_1}{0.5 \cdot (\Phi_1 + \Phi_2 + 2\Phi_S)} \qquad (1.2)$$

From the definition it is apparent that the subject contrast is governed by the integral photon attenuation along the beam line which is proportional to the cross section. The inherently low subject contrast for megavoltage EPID images is caused by the energy dependence of the photon-matter interaction processes involved. For kV-photons (as used in diagnostic imaging), the dominant contrast producing interaction is the photoelectric effect. For the photoelectric cross section, σ_{pe}, we have:

$$\sigma_{pe} \propto \frac{Z^3}{E^3} \qquad (1.3)$$

Here E denotes the incident photon energy and Z is the atomic number of the material. The effective atomic number Z_{eff}[14] is much higher for bone ($Z_{eff} = 13.8$) than for water ($Z_{eff} = 7.42$) (or soft tissue) resulting in good contrast between these media (Khan [32]). However, because of the strong energy dependence $\sigma_{pe} \to 0$ for megavoltage photons. In this energy range Compton scattering is the dominant interaction governing the contrast. The compton cross section is mainly dependent on electron density, i.e. $\sigma_c \propto \rho_{e^-}$ which is similar for bone and tissue ($\rho_{e^-}^{\text{bone}}/\rho_{e^-}^{\text{water}} \approx 1.66$)[15] resulting in the observed poor image contrast.

The spatial resolution is limited by the spot size of the imaging source. For megavoltage photon beams the spot size is typically in the range of several millimeters since they are optimized for radiotherapy rather than for imaging purposes.

The Varian AS-1000 EPID

The imager used for all portal image acquisitions in this thesis is a Varian AS-1000 electronic portal imaging device (EPID). It is mounted to the LINAC gantry by a robotic arm as depicted in Figure 1.5. The following table gives a summary of its specifications:

type	as1000, Varian Medical Systems
front plate (metal)	1 mm Cu
scintillator	$Gd_2O_2S : Tb$ (Kodak Lanex B)
image receptor	1024 x 768 AMFP
pixel spacing	$392\,\mu m \times 392\,\mu m$
maximal frame rate	12.86 Hz at 600MU/min and half-resolution

1.6   Outline of this thesis

This thesis is divided into three parts: in Chapter 2 an algorithm for markerless lung tumor motion estimation from megavoltage EPID images is presented and

---

[14]The *effective atomic number Z_{eff}* is defined as the average atomic number of a compound.
[15]$\rho_{e^-}^{\text{bone}} \approx 5.55 \times 10^{23}\ cm^{-3}$ and $\rho_{e^-}^{\text{water}} \approx 3.34 \times 10^{23}\ cm^{-3}$ (Khan [32])

tested on a dynamic thorax phantom as well as on EPID images acquired during SBRT treatment delivery to lung cancer patients. In Chapter 3 this algorithm is used to actively compensate tumor motion in real-time during radiotherapy delivery to a phantom with a dynamic multi-leaf collimator tracking system. Chapter 4 discusses the application of the algorithm presented in Chapter 2 to calculate delivered dose. A summary of the thesis as a whole along with conclusions are given in Chapter 5.

Publications and notes

The research presented in this thesis was carried out at the Brigham and Women's Hospital (BWH) / Dana-Farber Cancer Institute (DFCI) / Harvard Medical School in Boston, MA (USA). Chapter 3 was partially carried out at the University of Sydney, Australia.

Parts of this work have already been published in a peer reviewed journal (Rottmann et al. [52]) and at international conferences in form of oral presentations (Rottmann et al. [53; 54; 56]) and a poster (Rottmann et al. [55]). Chapter 4 has been published in a peer-reviewed journal with the thesis author as the 2nd author [3].

2 Real-time lung tumor motion estimation

Knowledge of the tumor location during radiotherapy treatment delivery is desirable for a range of applications aimed at quantifying and reducing the negative effect of tumor motion on the treatment outcome. In this chapter an algorithm is presented that uses 2D radiographs from beam's-eye-view perspective to calculate soft tissue displacement in real-time during radiation therapy delivery.

In Section 2.1 a review of available techniques with their respective benefits and drawbacks is given and a motivation for the approach followed in this thesis is given. The algorithm is described in detail in Section 2.2 and then characterized with experimental data in Section 2.3.

2.1 Motivation

We would like to have a motion analysis tool that can provide continuous real-time 3D position, rotation and deformation data for the volume of interest without adding any risks to the patient. However, all currently available methods make certain compromises to these requirements. In general all of them will operate on a discrete time metric and have a characteristic time needed for information processing. Current methods of tumor tracking can be divided in three categories:

External surrogate: The motion of the chest/abdomen is used as a surrogate to approximate the motion of the target volume. The basis of this technique is the assumption that surrogate and target motion are well correlated. However, Ionascu et al. [27] have found that this assumption may not always be valid. There are several systems commercially available based on this principle, all capable of real-time operation: The real-time position management (RPM) system (Varian Medical Systems, Palo Alto, USA) tracks retroreflectors attached to the patient's chest with an infrared camera, the Anzai Belt system (Siemens Medi-

cal, Erlangen, Germany) measures the chest expansion from respiration with the help of a pressure sensor and Gate CT / Gate RT (Vision RT) uses 2 cameras to reconstruct the patient's surface in 3D.

Internal surrogate: Fiducial markers implanted in proximity of the target volume can serve as robust and reliable internal surrogates. The underlying assumption of a strong correlation between internal surrogate and target volume motion as well as a stable marker location has been found to be (at least intra-fractionally) generally valid. However, there have been studies indicating that markers may not be stable over longer time frames. Imura et al. [26] for instance have report that markers implanted in the bronchial tree only stayed stable for about 1-2 weeks (which is sufficient for an SBRT course). For lung as the target site there is also a considerable risk for pneumothorax occurrence from the implantation procedure[1] which may not be clinically acceptable. Kupelian et al. [37] and Kothary et al. [35] report incidence rates of $> 40\%$ in their studies.

The position of radiopaque fiducial markers can be obtained from projection images by segmentation algorithms. Another approach uses a microscopic coil inside the fiducial for radiofrequency detection (e.g. Calypso Inc.).

Markerless Tracking: The motion of the target volume is estimated from projection images directly, i.e. without the help of an additional surrogate. The algorithms used may be further divided to classification algorithms and direct tracking algorithms.

$\rightarrow$ In *classification algorithms* a training data set is used to identify possible tumor locations and to build a feature set for identifying those tumor location states in subsequent images. The actual tracking process consists then of a classification process (SVM, regression, neural network, etc.) that tries to assign each projection image or external surrogate location to one of the previously defined tumor locations (Cui et al. [13], Xu et al. [73], Wu et al. [71], Lin et al. [39]). This approach lacks the ability to adapt to changes in the breathing pattern that cannot be described with the motion observed during the training session (extrapolation). However, it works well for the

---

[1]The pleural cavity, i.e. the space between the lung and the chest wall is filled with a liquid allowing the lung to expand and contract with minimal friction while not being directly attached to the inner chest wall. If air enters the pleural cavity, for instance through puncture from inserting fiducials with a needle, this is called *pneumothorax* and can cause the collapse of the adjacent lobe of the lung.

application of gated treatment, where it is not necessary to know the precise location, but rather to decide whether the target is within a predefined region.

$\rightarrow$ For *direct tracking* algorithms, a set of features is extracted and localized on each image frame. Although it may be difficult to find features suitable for tracking, a benefit of this approach is its robustness in the presence of irregular breathing patterns. This property makes the direct tracking approach highly desirable and therefore it is the approach used in this thesis.

The quality of the input images is crucial for the accuracy and robustness of a tracking algorithm. When compared to kV x-ray images, MV x-ray images are usually of inferior quality, i.e. low signal to noise ration (SNR) and low contrast to noise ratio (CNR) resulting in a comparatively poor soft tissue contrast (cp. Section 1.5.2). Also, the illumination level may change over time due to lung filling/emptying (Berbeco et al. [6]) and we have observed additional illumination changes on the first few portal images of a sequence.

Both radiopaque fiducial marker tracking as well as markerless tracking rely on projection images. Two devices that are commonly available in the treatment room are a fluoroscopy x-ray imaging system and/or a electronic portal imaging device (EPID). Most modern treatment machines feature both options. The fluoroscopic x-ray imaging system consists of an x-ray tube and a flat panel detector mounted to the clinical linear accelerator. The EPID is a flat panel detector that is capable of capturing the exit radiation of the treatment beam.

 If projection images can only be acquired from one direction, the geometry of the imaging setup becomes important as it determines the directions in which no position information is available. For tumor motion monitoring purposes the optimal setup will capture both directions of the sharp fluence gradient of the treatment beam and will for that reason be in line with the treatment beam (Nill et al. [47], Suh et al. [65]). This is illustrated in Figure 2.1. While kV x-ray imaging has the advantage of superior image quality and a higher frame rate compared to the commercially available MV-EPID systems there is at the time of this publication no kV-imaging equipment with beams-eye-view geometry commercially available. There is also some concern about the additional dose associated with kV fluoroscopic imaging. Winston et al. [70] and Murphy et al. [43] estimate a typical entrance dose-rate of 22 mGy/min and Shirato et al. [63] report similar surface values as well as roughly 4 mGy/min at 10 cm depth in the context of real-time tumor tracking during SBRT. In contrast, Kilby and Savage [33] have
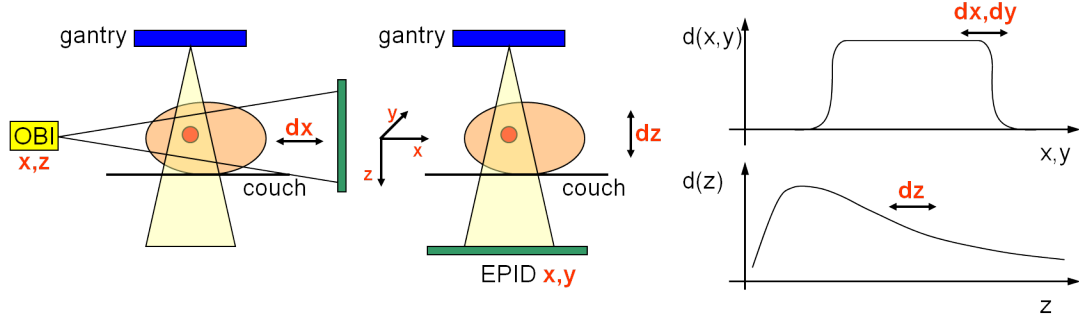
Figure 2.1: Implications of the imaging geometry: The 90° imager orientation *(left)* captures only one direction of steep dose falloff while the in-line setup *(right)* captures both. On the *(right)* qualitative depth dose curves for all directions are sketched.

shown that the additional dose to the patient from MV imaging, mainly from low-energy backscatter from the imager, is negligible when the EPID is placed more than 15 cm from the exit surface of the patient, a distance that is easily exceeded in practice (we used > 50 cm).

2.2   Soft tissue localization (STiL) algorithm

The STiL algorithm is designed to track soft tissue motion online and in real-time[2] during delivery of 3D conformal radiotherapy. Throughout the treatment continuously acquired MV-EPID images are used as input signal[3]. The schematic of the clinical setup is shown on the *(left)* of Figure 1.5. The algorithm needs to cope well with the inherent restrictions of using the EPID as described earlier, i.e. image quality (low SNR and CNR), limited field of view (treatment aperture) and low frame rate (maximally 12.86 fps (at half-resolution) with our currently available hardware). Also, we want to be able to track independently from prior knowledge if necessary.

To make the algorithm robust with respect to target deformations, rotations, and partial occlusions, this thesis follows the approach of tracking multiple autonomously defined feature points to estimate soft tissue motion: Given an initial

---

[2]real-time is meant here in the context of Chapter 3, i.e. with a systemic latency δt that is smaller than the acquisition frame rate.

[3]In principle other 2D projection imaging modalities could actually be used as well, but we only used beam's-eye-view images from the portal imager.
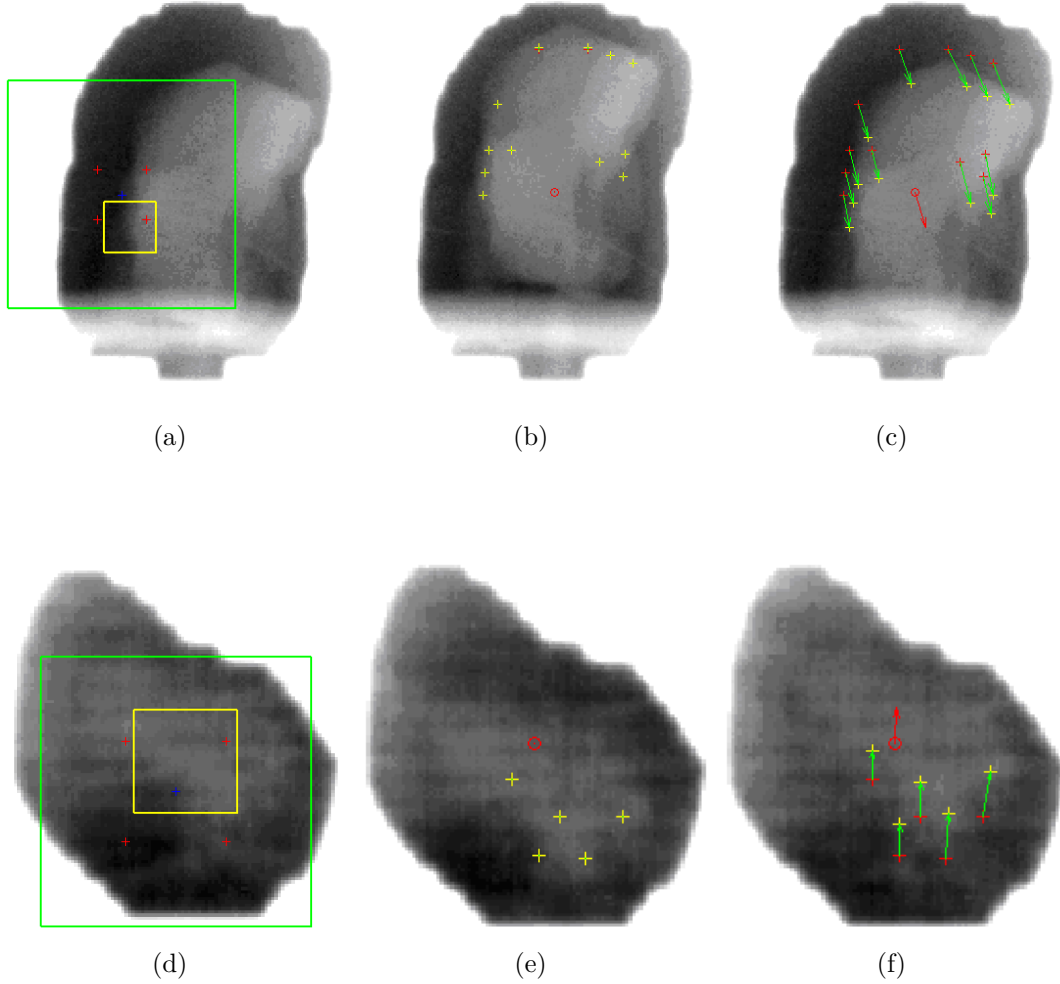
Figure 2.2: (a)-(c) Dynamic chest phantom, (d)-(f) Clinical data (SBRT treatment). (a),(d) Example of a template and its search region. The red crosses indicate the original position the yellow box the matched position and the green box the search region. (b),(c),(e),(f) Automatically defined landmark positions (red crosses), tracked positions (yellow crosses) and resulting tumor centroid mean offset (red arrow). Note that the red arrow only indicates an offset, not a position. The visible streak effects are most likely due to calibration issues of the portal imager.

gray value image I^* used as the origin and a sequence of images $\{I(t_i) \mid i \geq 1\}$ acquired at times t_i the the multi-region approach calculates a rigid soft tissue displacement vector $x(t_i)$ for each image with respect to I^*. The algorithm consists of three parts:

(i) A feature detector finds a set of landmark candidates on the reference image I^*, i.e. a set of points $\{p_j^* \mid j = 1, \ldots, N\}$ each surrounded by a small rectangular region $Q_{p_j^*} \subset I^*$ defined on the reference image I^*.

(ii) A tracking algorithm identifies on each subsequent incoming image $I(t_i)$ the locations $P_i = \{p_j(t_i) | j = 1, \ldots, N\}$ of all landmark candidates with respect to their initial positions $\{p_j^* \mid j = 1, \ldots, N\}$ defined on reference image I^*.

(iii) To limit the impact of tracking failures, a geometric regularization is applied to the set of new landmark candidate positions P_i reducing it to a smaller set $\widehat{P}_i \subset P_i$. The final result is the average displacement vector $x(t_i) = \langle \widehat{P}_i \rangle$.

Figure 2.2 provides sample MV-EPID images from a phantom study and from a lung SBRT delivery. Therein landmark region, search region and landmark displacement vectors are illustrated.

Landmark selection

In order to enable reliable tracking, each landmark region (feature), $Q_{p_j^*}$, needs to be uniquely identifiable on all images $I(t_i)$ at least within a small search region $S_{p_j}(t_i) \subset I(t_i)$. Thus, the quality of a landmark will mainly depend on how unique its texture/pattern is and how well its motion represents the tumor motion. For the latter, we assume that any motion visible within the field of view will be strongly correlated to the target volume motion. Hence one may use any moving structure as a surrogate for the tumor motion and it is sufficient to restrict the landmark search to a local texture analysis of the image I^* chosen to be the origin for the tracking. To reduce noise effects on the texture analysis a median filter and/or gaussian filter may be initially applied to I^*.

The local texture is analyzed by means of a local variance filter (Roesch et al. [51]):

$$Var(Q_{p_j^*}) = \frac{1}{M-1} \sum_{\xi \in Q_{p_j^*}} \left(Q_{p_j^*}(\xi) - \overline{Q}_{p_j^*} \right)^2 \qquad (2.1)$$

Here $Q_{p_j^*}$ is a small region, centered around pixel p_j^*, containing M pixels. $\overline{Q}_{p_j^*}$ is the mean value of all pixels within $Q_{p_j^*}$. High gray value variance is taken
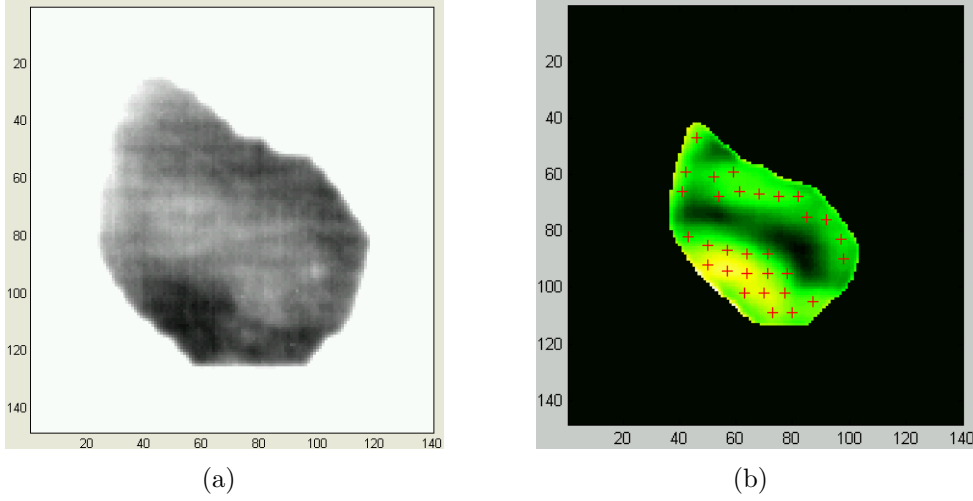
Figure 2.3: Automatic landmark generation on MV-EPID images: (a) original MV EPID image (only the window/level has been adjusted to make the tumor visible), (b) variance filtered image with 30 local landmark candidates. Note that the soft tissue contrast is maximal at the boundary of the tumor mass, while it is minimal within the tumor mass.

as a measure of high local texture around pixel p_j^*. Eq. (2.1) can be efficiently computed when rewritten as a convolution in the spatial domain which allows computation as a multiplication in the frequency domain. $Q_{p_j^*}$ was chosen to be the same size as the landmark regions. An example of a variance map for a sample image is shown in Figure 2.3.

Local maxima of the variance filtered origin image are taken to be potentially suitable landmark candidates. To reduce bunching, landmarks are constrained to have a minimal distance between each other. The underlying assumption that high gray value variance is uniquely correlated with important tracking structures may not always be true though. Besides noise effects, which can be reduced by the application of an initial median or gaussian filter, sharp straight edges can cause a problem as they show a high texture value but are not unique (cp. aperture problem in Jähne [28]). To reduce this effect and ensure each landmark is unique within a small neighborhood, a self similarity map based on *normalized cross correlations* (NCC) is calculated for each feature point. The gaussian curvature at the zero position is taken as an indicator for edginess, i.e. it is assumed, that the similarity for a straight edge is going to be smaller than for a unique feature.

Each landmark consists of a small image region $Q_{p_i^*}$ and a surrounding search region S_{p_i}. To minimize computation time of the tracker and to maximize uniqueness of the landmark, the search region is chosen to be asymmetric, i.e. the longer side in the superior-inferior image direction where the most prominent motion is expected. These parameters can be chosen as fixed values as long as they can cover the entire motion range (estimated, for example, from a 4DCT, other pretreatment imaging or generically assuming $20\,\text{mm}$ [60]). However, for non-coplanar fields[4] the search box dimensions that need to be projected to the imager plane are assigned as (in EPID image coordinates):

$$s = \begin{bmatrix} x \\ y \end{bmatrix}_{g,c} = \begin{bmatrix} s_{si} \cdot \sin\left(\phi_c\right) \cdot \cos\left(\phi_g\right) \\ s_{si} \cdot \cos\left(\phi_g\right) \end{bmatrix} \tag{2.2}$$

Here the indices G and C stand for gantry and couch, respectively and s_{si} stands for the superior-inferior motion range. An appropriate minimal value $x, y \leq \kappa$ is assumed.

Tracker

The input for the tracking algorithm is a new image $I(t_i)$ acquired at time t_i, a set of search window positions $\{s_j | j = 1, \ldots, N\}$ and a set of landmark regions $Q(p_j^*) \subset I^*$ as defined on the initialization image I^*. The new landmark position is calculated by finding the overlap position of landmark region and search region that maximizes a given similarity measure.

There exist several similarity measures that are commonly used for the application in 2d matched filter algorithms. We tested both Normalized Mutual Information (NMI) and Normalized Cross Correlation (NCC). However, the NMI is a statistical measure and therefore depends on the sample size. Our image resolution is too low to allow reasonably sized templates working with this measure. Also NMI implementations are usually significantly slower than NCC. On the other hand NCC can be efficiently implemented to meet our time constraints. The normalized cross correlation coefficient for a landmark region $Q_{p_j^*}$ and a

---

[4]A field is called non-coplanar if the treatment couch is rotated.

search region $S_{p_j^*}$ is defined as:

$$S_{NCC}(x,y) = \frac{\sum_{u,v}\left(Q_{p_j^*}(u,v) - \overline{Q}_{p_j^*}\right)\cdot\left(S_{p_j}(u-x,v-y) - \overline{S}_{p_j}\right)}{\sqrt{\sum_{u,v}\left(Q_{p_j^*}(u,v) - \overline{Q}_{p_j^*}\right)^2\cdot\sum_{u,v}\left(S_{p_j}(u-x,v-y) - \overline{S}_{p_j}\right)^2}} \qquad (2.3)$$

Here $\overline{Q}_{p_j^*}$ is the mean value over all pixels in the landmark region and $\overline{S}_{p_j}$ is the mean value over all pixels in the search region that overlap with the landmark region. As recommended by Lewis [38], we precompute the mean values in the numerator and denominator of Eq. (2.3). Then the NCC can be computed as a simple multiplication in the frequency domain:

$$S_{NCC}(x,y) = \mathcal{F}^{-1}\left\{\mathcal{F}(Q_{p_j^*})\cdot\mathcal{F}(S_{p_j})^*\right\} \qquad (2.4)$$

Here $\mathcal{F}(S_{p_j})^*$ is the complex conjugate of the Fourier transform of the search region S_{p_j}. With Eq. (2.4) the NCC is calculated for all possible pixel shifts of the template within the search region at once, resulting in a similarity map. The location of the maximum on this map corresponds to maximum correlation, i.e. the best-match position. The output of the tracker is the set of displacement vectors $\{p_j(t_i)|j=1,\ldots,N\}$.

Regularization

Robust regularization is essential because tracking failures of some landmark regions may be expected on each image for several reasons:

- landmark candidates are chosen solely based on the texture measure without considering temporal gray value gradient, i.e. there may be landmark candidates that are pinned to static structures contained in the candidate set.

- landmarks that are attached to a structure that is not unique.

- occlusion caused by the restricted field of view (landmark gets partially occluded at times when wandering outside the treatment aperture)

- unfavorable deformation that causes the landmark to lose its uniqueness within the search window.

The regularization works as follows: once a set of initial landmark positions $\{\,p_j^* \mid j=1,\ldots,N\}$ has been selected their relative geometric relationships are

(a)   (b)   (c)
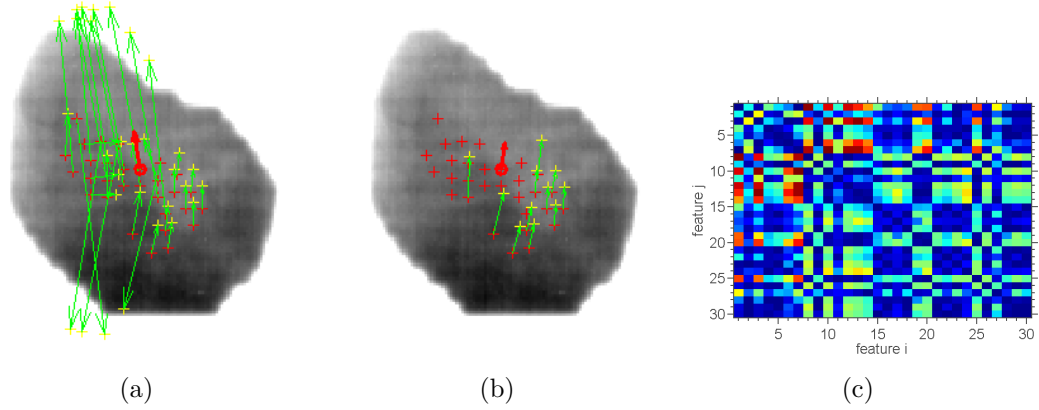
Figure 2.4: Illustration of the regularization method for a case with $N = 30$ landmark candidates. (a) and (b) show EPID images acquired during lung SBRT delivery of a patient. The position of each landmark candidate $\{p_j^* | j = 1, \ldots, N\}$ on the initialization image I^* is marked with a red cross and the individual displacement vectors $p_j(t_i)$ are drawn in green. The average displacement vector $x(t_i)$ is drawn as red arrow in the center. In (a) the displacement vectors of all landmark candidates are shown before regularization (b) after regularization. In (c) A_{ij}^t is depicted as color coded matrix: blue refers to small deviations, red to large deviations.

stored as a symmetric $N \times N$ matrix

$$A_{ij}^* = \|p_i(t_0) - p_j^*\| \tag{2.5}$$

On each subsequent image the new landmark positions are expected to have a similar geometric relationship to each other as on the initialization image. The deviation from the initial relation can be calculated for $t > 0$ as another symmetric matrix:

$$A_{ij}(t) = \|\ A_{ij}^* - \|p_i(t) - p_j(t)\|\ \| \tag{2.6}$$

While a certain degree of deformation and rotation are allowed, the relationship of the landmarks should stay similar to the initialization image. This is used as regularization criterion: the landmark with the greatest value of

$$a_j(t) = \sum_i \frac{A_{ij}(t)}{N^2} \tag{2.7}$$

that is larger than a threshold is removed from the landmark set for the current image and not used for calculation of the average motion trajectory. Landmarks are iteratively removed until the values are below a threshold and we are left with a subset $\{p_{j_k}|j_k = 1, \ldots, N(t_i)\}$. Here $N(t_i)$ is the current number of landmarks remaining on image $I(t_i)$ after regularization is applied. An example illustrating this procedure is depicted in Figure 2.4.

From the $N(t_i)$ remaining landmarks for image $I(t_i)$ an average displacement vector $x(t_i)$ is calculated which is the final output of each acquisition loop.

$$x(t_i) = \frac{1}{N(t_i)} \sum_{j_k} p_{j_k}(t_i) \tag{2.8}$$

Figure 2.4 gives an example illustrating the rejection of failing landmarks by means of the regularization procedure that has been described here.

Implementation and Graphical User Interface

The STiL algorithm is implemented in Matlab$^{\circledR}$. To enhance the performance of the tracking loop, the normalized cross correlation computation is implemented in C++ with the help of the open source computer vision library *OpenCV*. For faster image acquisition a frame grabber with a basic C++ API was provided by Varian Medical Systems (Palo Alto, CA, USA). It allows us to circumvent, at least in the phantom studies, the memory restrictions imposed by the treatment software system. The tracking loop of the STiL algorithm can be executed in real-time for an acquisition frequency of up to 12.86 Hz. This is discussed in detail in Chapter 3.

Two graphical user interfaces were developed: one geared towards a retrospective interactive testing platform and one for visualization during real-time tracking. The first *GUI* allows the user to interact with all parts of the algorithm, track tumors manually with tools developed for this study, explore each template and its similarity map individually and interactively adjust the window/level. A screenshot of the first *GUI* is shown in Figure 2.5; the second *GUI* is shown in Figure 3.3.

(a)   (b)
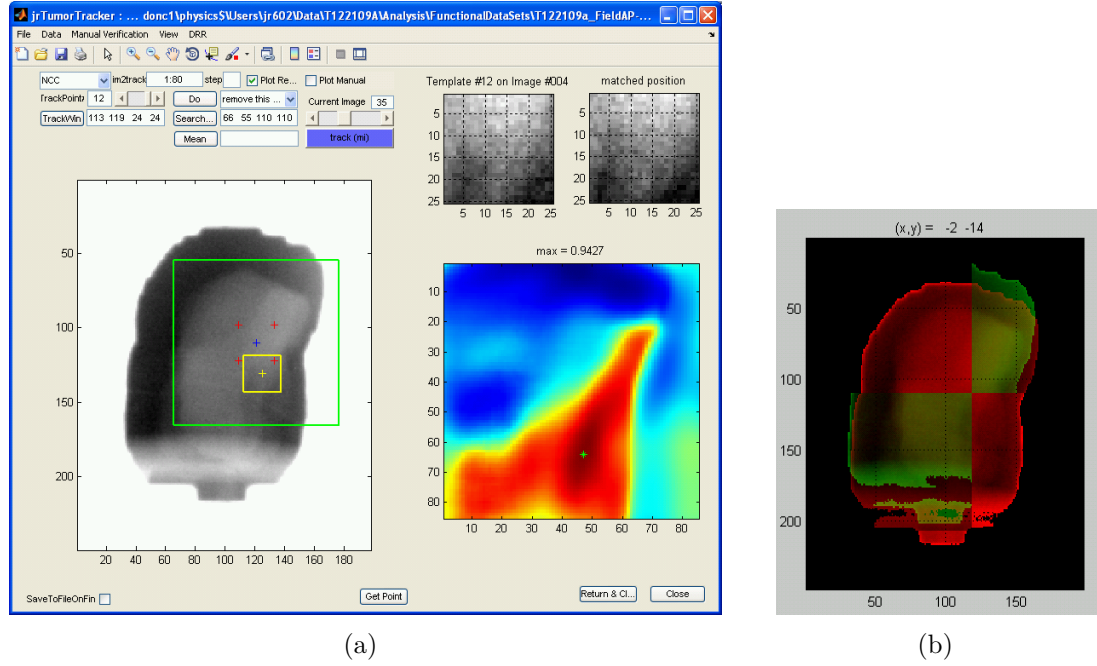
Figure 2.5: Graphical User Interface (GUI) used to browse tracking results and
define manual reference trajectory: (a) On the left is the original image (cropped
to the treatment aperture) shown. The green rectangle is the search region, the
reference landmark region location is marked in red, the matched one in yellow.
The colorwash on the right is the similarity map and the green cross indicates the
maximum, i.e. best matching location on the current image. (b) Manual tracking
tool. The red image is the reference image, the green one can be moved with the
mouse to match the red one. Opacity and opacity pattern can be adjusted by
the user with the mouse.

2.3   Characterization of geometric accuracy

In order to characterize the algorithm's accuracy it has been tested online with a dynamic chest phantom as well as retrospectively with patient data from SBRT treatments monitored with the EPID at the Dana-Farber Cancer Institute (Boston, USA). All data was acquired with a beam energy of $6MV$ on a Varian Trilogy TX featuring an AS-1000 amorphous silicon electronic portal imager. While the hardware supports a raw resolution of 1024×762 pixels, data was acquired at half resolution (512×382) to decrease memory requirements. This was particularly important for image acquisition during patient treatments because the vendor's software did not allow the allocation of sufficiently large image caches without system crashes.

To quantify the mean tumor centroid trajectory $p^{(a)}(t)$ calculated by the tracking algorithm an expert made a reference trajectory $p^{(m)}(t)$ by manually matching the gross tumor volume (GTV) of a reference frame to all other frames in the portal image sequence. Since it can be difficult (even for a human observer) to clearly distinguish the GTV on portal images, the examiner was given the freedom to choose any region containing visible structures of the tumor and exhibiting maximal motion. To measure the consistency of the verification tumor trajectory, the set of portal images presented to the human observer included redundancies. The standard deviation over all tumor centroid locations determined on a single image was calculated. Also, the order in which the images were presented was randomized to avoid any possible bias. We define the automatic tracking error as the difference between automatic and manual position, i.e.

$$\Delta^{(a)}(t) = \left\| \, p^{(m)}(t) - p^{(a)}(t) \, \right\| \tag{2.9}$$

and the manual tracking uncertainty as its standard deviation

$$\Delta^{(m)}(t) = \sqrt{\frac{1}{N(t) - 1} \sum_{i=1\ldots N(t)} \left(p_i^{(m)}(t) - p^{(m)}(t) \right)^2} \tag{2.10}$$

Here $\Delta^{(a)}(t)$ is the uncertainty of the tracking algorithm, $\Delta^{(m)}(t)$ is the verification uncertainty, $N(t)$ is the number of times image $I(t)$ was presented to the examiner, $p_i^{(m)}(t)$ is the verification location at the i-th repetition and $p^{(m)}(t)$ is the average verification location over all repetitions.
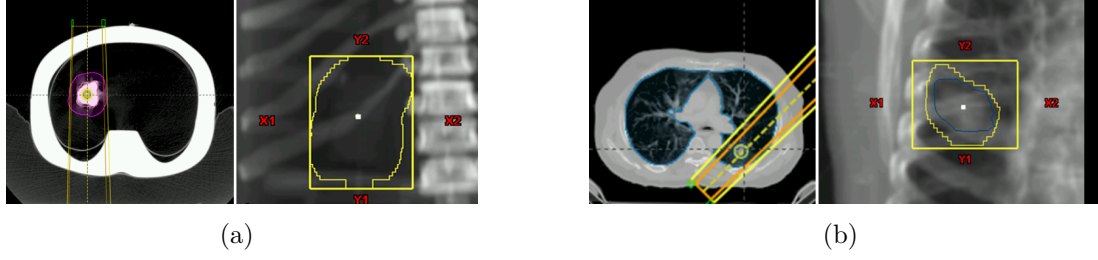
(a) (b)

Figure 2.6: Setup for experimental verification: (a) The dynamic thorax phantom is set up to an *anterior-posterior* (AP) field. (b) Example of a patient setup – here for a *right posterior-oblique* (RPO) field. The *(left)* sides (a) and (b) shows the beam setup as seen in the treatment planning software. the *(right)* sides show the respective *digitally reconstructed radiographs* (DRR) with the planned MLC leaf positions. For the patient, the ITV contour is overlaid in blue.

The overall performance of the tracking algorithm on an entire image sequence of N images in terms of geometry accuracy is measured by the root mean square error:

$$RMSE = \sqrt{\frac{\sum_{t_i}(\Delta^{(a)}(t_i))^2}{N}} \tag{2.11}$$

Figure 2.6 shows the experimental setup for both, dynamic thorax phantom and patient data acquisition.

2.3.1 Geometric accuracy on phantom data

 For the phantom study an anatomically realistically shaped dynamic chest phantom was used (see Figure 2.7(a) and (Court et al. [12])). It consists of a torso that has an anatomically correct inlay (bones made from solid water). To simulate respiratory motion, the torso's lungs are inflated/deflated with pressurized air while a tumor mass mounted on a stick is moved in the superior-inferior direction by a separate motor. Both motions can be programmed independently. The phantom tumor mass was modeled after the GTV extracted from a patient CT and manufactured by rapid prototyping with a flexible resin (see Figure 2.7(b)). The appearance of the phantom tumor in kV and MV images is very similar to real patient images. The average CT number of the model tumor is 76 (at 120kVp), compared with 30 for the real patient (an effective difference in electron density of 2%). Its physical density and hardness are specified as 1.3 $\mathrm{g\,cm^{-3}}$ and

(a)   (b)
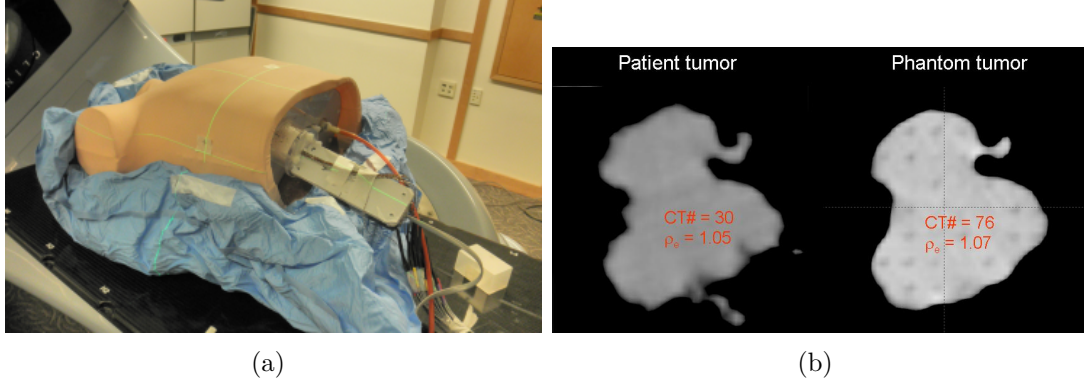
Figure 2.7: (a) Dynamic chest phantom on the treatment table. The blue body bag is used to have a more reproducible setup on the treatment table (and CT scanner) - this device is also frequently used for lung SBRT patient setup. (b) CT images of the original tumor and the model used in this study.

(a)   (b)
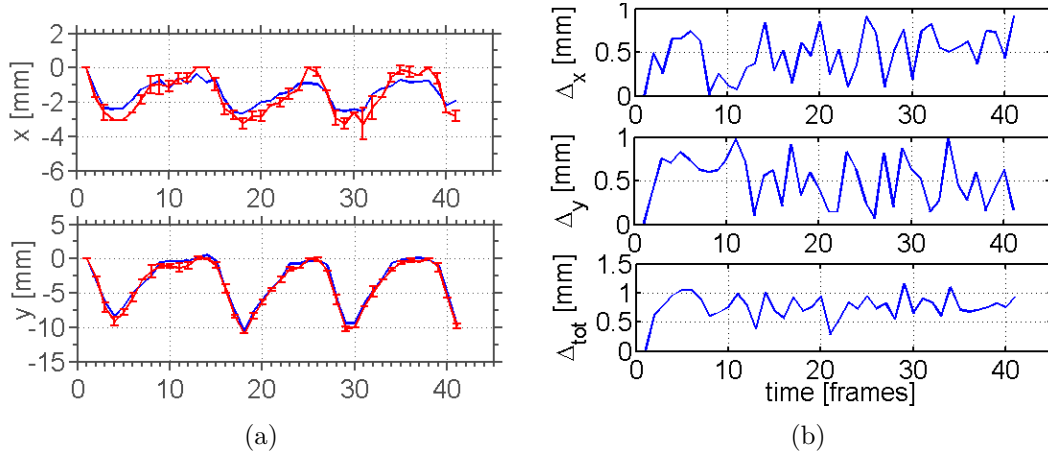
Figure 2.8: Geometric accuracy of STiL algorithm on phantom data: A sample trace recorded with the dynamic thorax phantom is shown in (a). The manual verification curve is depicted in red, with the error bars being the user variability. The blue curve is the output of the algorithm. The absolute error is shown in (b), the root mean square error computed to $(0.8 \pm 0.2)\,mm$

27 durometers, respectively – the hardness for real tumors ranges 0-60 (Belyaev et al. [4], Bloom et al. [9]), respectively.

While this phantom is the most realistic available, it is still an approximation of reality due to a lack of deformation (shearing) and the relatively high tumor-tissue contrast. However, it is an excellent tool to study the baseline performance of the proposed tracking algorithm.

The phantom was programmed with internal / external motion data obtained from implanted fiducial marker tracking during lung SBRT treatments at the NTT Hospital in Sapporo, Japan (Shirato et al. [62], Berbeco et al. [7]). The motion amplitude was in the range of $10\,mm$ and the pixel size (at isocenter) was $0.436\,mm \times 0.436\,mm$ (which represents half resolution images).

Results

A comparison of the tracking algorithm and the manual verification registration for 42 portal images of an AP field is shown in Figure 2.8 ($\phi_g = 0°$, $\phi_c = 0°$, 2 fps at $800\,mm$ vertical imager-isocenter distance). The tracking result is plotted on the left: blue for image x and y direction together with the manual verification in red for comparison. The error bars are derived from the standard deviation of the repeated manual registration for each frame. The accuracy of the prospective tracking implementation is found to be $\Delta^{(a)}(t_i) < 1\,mm$ with a $RMSE = (0.8 \pm 0.2)\,mm$.

2.3.2 Geometric accuracy on patient data

A typical lung SBRT treatment course at the Brigham and Women's Hospital / Dana-Farber Cancer Institute consists of 9 - 11 conformal treatment fields, some of which may be non-coplanar. The prescription dose is either 54 Gy delivered in 3 fractions or 60 Gy delivered in 5 fractions. In all cases, 6 MV photon beams are used. The treatment setup is accomplished in multiple steps, including patient alignment in a stereotactic body frame, laser-guided setup of the frame to the treatment room coordinates and registration of bony landmarks in stereoscopic kV radiographs before a final 3D soft tissue manual registration with cone-beam computed tomography (CBCT) is performed. During treatment delivery, the AS-1000 EPID (Varian Medical Systems, Inc) is moved to $800\,mm$ vertical distance from the isocenter and operated in cine mode with half resolution at a frame rate of 2 fps resulting in a pixel spacing of $0.436\,mm$ in the isocenter plane. Each
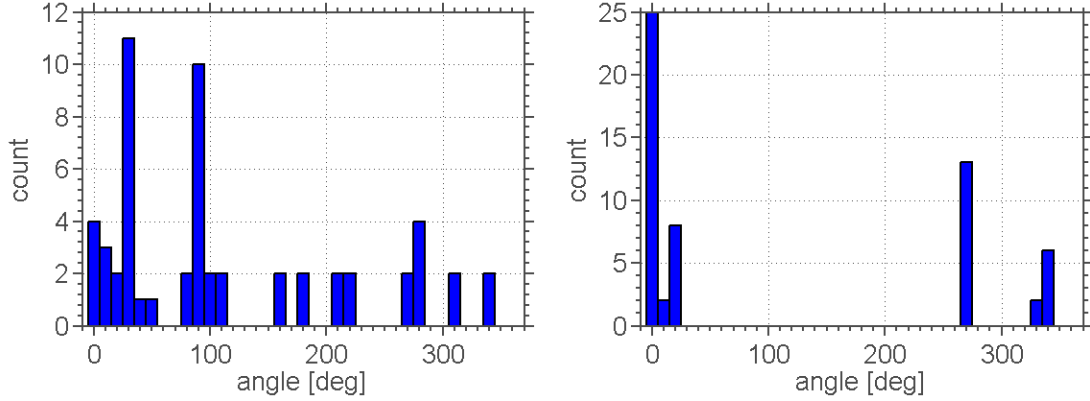
Figure 2.9: Histograms for the gantry angles *(left)* and couch angles *(right)* of the analyzed patient data. The gantry angles $\phi_g \neq 0$ denote "non-coplanar" fields.

frame is an average of four frames to enhance the signal to noise ratio (SNR). The improvement in SNR outweighs any introduction of motion blurring. For our study, in-treatment EPID images were successfully acquired for all treatment fields of 9 lung SBRT treatment courses (19,942 portal images). This included non-coplanar geometries. Although there was no pre-selection of the patients, in order to establish a gold standard with which to compare the tracking, we only included beam angles in the study for which an expert examiner was capable of performing manual tracking, i.e. a minimum of visibility and motion was required. A histogram of the beam angles and RMSE is given in Figure 2.9. 54 fractions from 34 beam angles were used for analysis with the first 40 images of each fraction taken for verification, i.e. manual registration. A total of 2,182 images were manually registered to the respective first image in each fraction. To minimize bias and to obtain a measure of reproducibility for the manual registration, the images were presented in random sequence and each image was shown 3 times.

Results

For the manual registration, a total of 6,546 portal cine EPID images (including repeated images) were analyzed by an expert viewer. Figure 2.10 shows a sample consisting of three fractions of an AP field with couch kick of 270°. In this sample the tumor motion range in the superior-inferior direction is 13.1 mm and the tracking error is $< 2.3\,$mm at all times while the average rms-tracking-error is $(0.9 \pm 0.7)\,$mm. It is apparent from Figure 2.10 that each fraction does
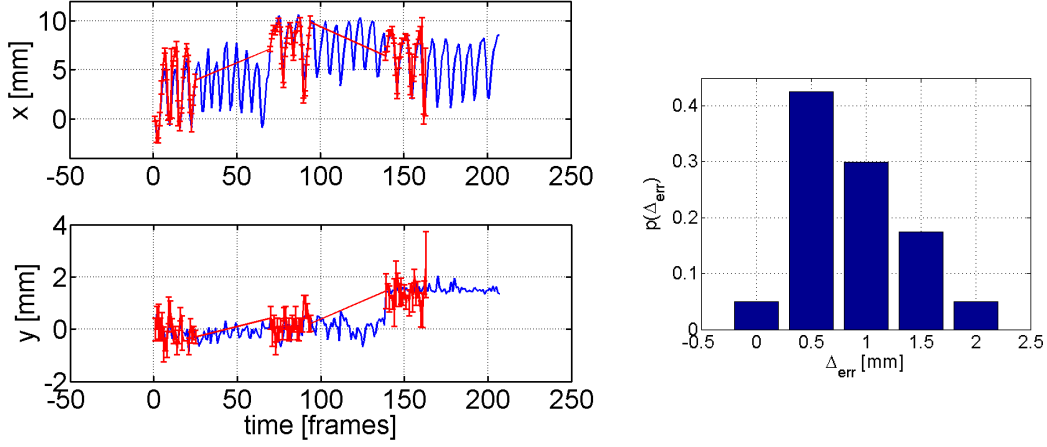
Figure 2.10: Sample trace of 3 fractions for a field with $\phi_g = 30°$ and $\phi_c = 270°$ *(left)*: the manual tracking result taken as gold standard (red) is overlaid with the algorithmic tracking results (blue). The error bars are the standard deviation of the manual tracking. $RMSE = (0.9 \pm 0.7)\,mm$. The tracking error distribution (normalized to unity) is shown on the *(right)*.

not necessarily follow a similar breathing pattern. The breathing motion does actually not have to follow any pattern at all as can be seen from Figure 2.12; the motion range in the superior-inferior direction is 24.4 mm here. While the error at each point in time is a good measure for accuracy validation, for dosimetric lung SBRT verification and adaptive radiotherapy the most important measure is the summed tracking error over time. We choose histograms to reflect this for each field/fraction/patient as well as for all patients. Figure 2.10 (right) shows an example for a single treatment field consisting of three fractions. In Figure 2.11 the overall $RMSE$ distributions for manual tracking, no tracking at all and automatic tracking are compared. The tracking accuracy is better than the location uncertainty in the case of not tracking while it is not quite as good as a human expert examiner, provided that our technique for estimating the error of the expert examiner is appropriate. The rms tracking accuracy of the marker-less algorithm was found to be $(2.1 \pm 1.7)\,mm$. Excluding the worst 9 series (out of 56) reduces the rms-error to $(1.5 \pm 1.1)\,mm$. Without any tracking the rms-error would have been $(3.9 \pm 2.7)\,mm$ and the rms-uncertainty of the manual tracking was found to be $(0.9 \pm 0.5)\,mm$.
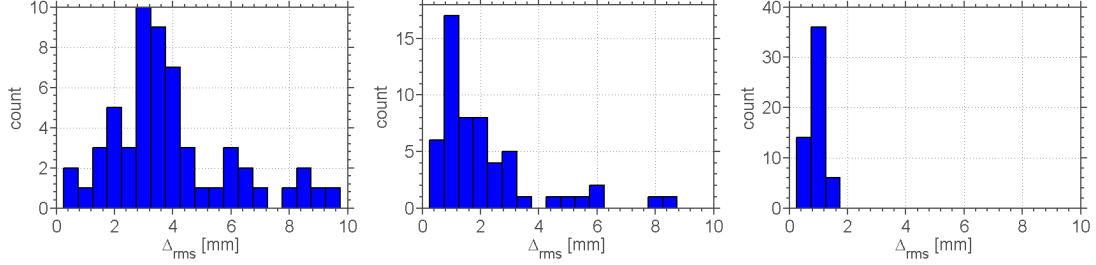
Figure 2.11: The top row shows the distribution of the rms-error from tracking 9 patients: no tracking, tracking algorithm, manual tracking (from left to right).
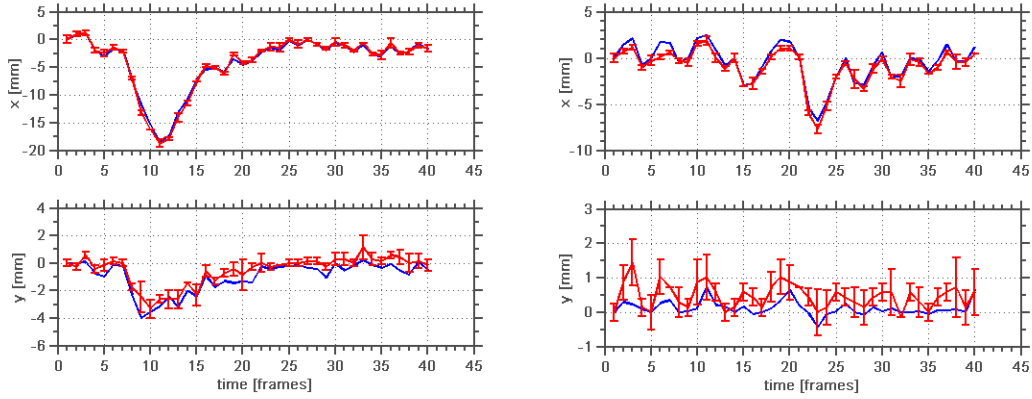
Figure 2.12: An example for irregular breathing patterns (of a patient): patient 01, fractions 1 and 2. The manual tracking result taken as gold standard (red) is overlaid with the algorithmic tracking results (blue). The error bars show the variablility of manual tracking. The motion appears to be picked up well resulting in an rms-error of (0.7 ± 0.2) mm. Also, notice that this is a non-coplanar field geometry with couch angle $\phi_g = 270°$, i.e. the superior-inferior direction is parallel to the image x-direction.

2.4   Discussion

There are several factors that may influence the performance of the real-time tracking algorithm. First, we assume that any moving soft tissue within the treatment aperture is an adequate surrogate for the tumor motion, i.e. there could be cases in which the visible motion is not generated in the tumor plane but above or below. As we are analyzing projection images we do not have any depth information available. However, this may be addressed by analyzing the pretreatment 4DCT commonly used for planning. There is good reason to believe that maximal texture appears at the border of lung tissue / tumor tissue. Most of the fractions that failed in our study ($RMSE > 3\,mm$) did so due to the fact that the tumor moved too far out of the aperture, resulting in an insufficient number of landmarks for tracking. For these cases it would be helpful to incorporate other information such as external surrogate tracking (e.g. Vision RT, *real-time position management* (RPM), Varian Medical Systems or the Anzai belt, Siemens Medical) or priors from the pre-treatment 4DCT and CBCT.

The accuracy of the algorithm in its current implementation also depends on the quality of the first EPID image in the sequence. Since all subsequent images are measured as an offset to this first image, problems with the first image may introduce a systematic error. Updating the correlation may be a suitable approach to address this problem in the future.

Another point of influence for the tracking accuracy is the parameter selection in the algorithm, e.g. number of initially selected candidates, number of landmarks tracked on each image (before regularization), landmark region dimensions and search box dimensions We used one universal set of parameters for all cases to ensure comparable results. The only parameter that is automatically adapted to each treatment field is the search box dimensions, which are governed by Eq. (2.2).

2.5   Conclusions

We have developed a multi-region markerless lung tumor motion estimation algorithm and applied it in phantom as well as in patient systems. While the algorithm investigated works very reliably on physical phantoms with realistic breathing motion it may not yet be applicable out of the box in a clinical situation. However, it appears to be a good candidate for further investigation if

the hardware is improved for better image quality and higher image acquisition frequency.

3 Image guided radiotherapy with STiL

In Chapter 2 an algorithm for soft tissue motion estimation from continuously acquired MV-EPID images was described. In this chapter an application to *image guided radiation therapy* (IGRT) is presented: we integrate the *soft tissue localization* (STiL) algorithm with *dynamic multi-leaf collimator* (DMLC) tracking software developed for the Varian platform (Sawant et al. [58]) and a frame grabber device (*Matrox Solios eV-CL*) customized by Varian Medical Systems to enable real-time image acquisition with their LINAC-integrated image acquisition platform (IAS3).

Section 3.1 motivates the concept of motion compensation with a dynamic multi-leaf collimator and puts our approach to this into context with other concepts that have already been briefly reviewed in Chapter 1. Section 3.2 gives a detailed description of our experimental setup, integrating the STiL algorithm with the other components. Experimental evaluation of the concept using a dynamic phantom driven by breathing traces recorded from patients during lung SBRT delivery is presented in Section 3.3. In Section 3.4 the inherent issue of system latencies and their impact on the geometric accuracy of motion compensation systems is discussed in detail. A short overview of forward prediction algorithms to overcome latencies is given and the reduction of geometric error with the linear predictor actually used for the experiment is characterized using internal and external motion traces. Section 3.6 explores the application of the DMLC tracking concept in combination with a reduction of the treatment aperture during treatment delivery to spare more healthy tissue. A chapter summary is given in Section 3.6 and conclusions are drawn.

3.1   Introduction

Intrafractional target motion causes a blurring of the target dose distribution which necessitates the irradiation of additional normal tissue surrounding the tumor volume to achieve full dose coverage of the target and therefore local control
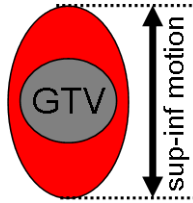
Figure 3.1: To ensure full coverage of the target area (GTV in gray) with the therapeutic x-ray beam despite the target's motion the aperture of the x-ray beam is opened up to the red area. However, this also increases the dose delivered to healthy tissue which limits the dose that can safely be delivered without causing serious side effects. Therefore it would be advantageous if one could follow the target area's motion with the radiation beam.

(see Figure 3.1). Thoracic and abdominal tumors often exhibit large respiratory motion ranges in the centimeter range (Ekberg et al. [15], Seppenwoolde et al. [60], Keall et al. [31]). At the same time stereotactic body radiation therapy (SBRT) for non-small cell lung cancers (NSCLC) has been found to be a promising alternative treatment option to surgery (Fakiris et al. [17]), particularly for early stage NSCLC and inoperable cases. However, due to the high doses per fraction (cp Chapter 1.3) administered in SBRT treatments large safety margins would be a huge concern for normal tissue radiation toxicity. As an example, to underline the seriousness of the concern about normal tissue toxicity a phase II clinical trial by Timmerman et al. [68]reported may serve : 8% of the patients died in connection to radiation toxicity.

Hence, there is in this context great interest in techniques capable of mitigating (intrafractional) tumor motion. However, neither the breathhold[1] nor the compression plate technique can reliably achieve a sufficient reduction of residual tumor motion and respiratory gating has the disadvantage of greatly extending the duration of the treatment. Beam tracking, however, can "freeze" the tumor motion by following it with the treatment beam itself. This has been previously proposed [30]. The procedure may be divided into two separate steps:

(i) A method for real-time target motion estimation.

(ii) A device to shift the radiation beam synchronized to the target position.

The main challenge for step (ii) was to develop a system with acceptable technical specifications concerning leaf position accuracy, velocity and response time. There are currently 2 research platforms [66, 58] that provide real-time adjustment of the treatment aperture in response to the signal of a motion capture

---

[1]See also Chapter 1 for a list of available techniques for tumor motion management.
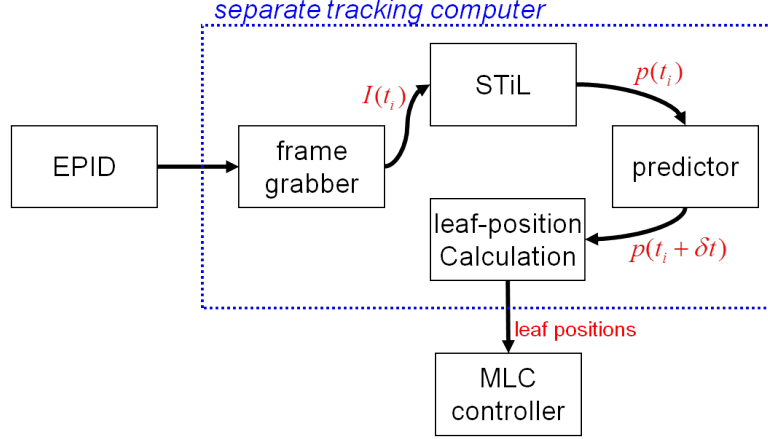
Figure 3.2: Data flow for the integration of frame grabber, STiL algorithm and DMLC tracker on the Varian platform. All non-clinically approved tools are bundled on a separate computer that receives image data as input through a high density connector cable and provides output in form of leaf position requests to the MLC controller.

device.

Other publications have utilized fiducial marker tracking for step (i). Both, the use of electromagnetically excitable markers (Calypso$^{\circledR}$) as well as marker segmentation from x-ray fluoroscopy images has been tested. However, as alluded to in Chapter 1 implanting fiducial markers in the lung carries a high risk of pneumothorax. Using the MV-EPID with soft tissue localization can avoid this obstacle and can at the same time also avoid the exposure of the patient to any additional dose since the treatment beam itself is used for imaging.

We therefore employ the STiL algorithm described in Chapter 2 for step (i) and a DMLC tracking system developed for the Varian platform [58] for step (ii).

,

3.2　System implementation on Varian platform

A system integrating fast image acquisition, real-time markerless image-based target position estimation, a linear predictor and a DMLC tracking system developed for the Varian platform (Sawant et al. [58]) was built. In Figure 3.2 a flowchart of this system is shown.

The frame grabber (*Matrox Solios eV-CL*) was provided by Varian Medical Sys-

tems, Inc. together with research software (iTool) to give RAM buffer access to their LINAC-integrated image acquisition system (IAS3). When compared to saving the images first on disk (cp. Fledelius et al. [19], Poulsen et al. [48]), the iTool can reduce the time ΔT_{aq} needed for image acquisition. The iTool research software features both a C# and a C++ *application programming interface* (API) giving programmatic access to the frame buffer. We chose the C++ API to allow for an easy binding to the STiL component which was written in Matlab® and C++. Acquired frames are pushed to Matlab® through a callback function that can be assigned with the API as soon as they become available.

The STiL algorithm is embedded together with the prediction algorithm in a Matlab® GUI to have real-time visual feedback for the user. The gui has an interface accepting incoming frame buffers pushed over from C++. It is shown in Figure 3.3 with the tumor model used for all phantom experiments. The resulting target positions $p(t_i)$ (red arrow in the figure) are fed into the predictor that uses the first N_t positions for training. The forward predicted position $\hat{p}(t_i + \delta t_s)$ is sent as a plain text message via *User Datagram Protocol* (UDP) to the DMLC component which calculates and then requests the new leaf-positions by communication with the MLC controller.

3.3   Characterization of implementation

The system latency and expected geometric accuracy of the integrated system, as described in Section 3.2, are measured with the help of a programmable dynamic phantom (*Washington University 4D phantom*) using the same realistic lung tumor model used in Section 2.3.1 as a phantom target. The *Washington University 4D phantom* consists of 3 translation stages mounted orthogonally to each other, allowing the motion of a tray of solid water on arbitrary motion trajectories in 3 dimensions. The phantom trajectory positions are sampled at a frequency of 50 Hz, exceeding the imaging system's maximally available frame rate of about 13 Hz. As an additional feature, an independent fourth axis can be driven to simulate the motion of an external surrogate.

Aperture position segmentation

To evaluate latency and geometric accuracy, it is necessary to measure the target position $p_{gtv}(t)$ and the aperture position $p_{mlc}(t)$ at the same time. This can be easily done from the EPID images as they contain both, the target and the MLC
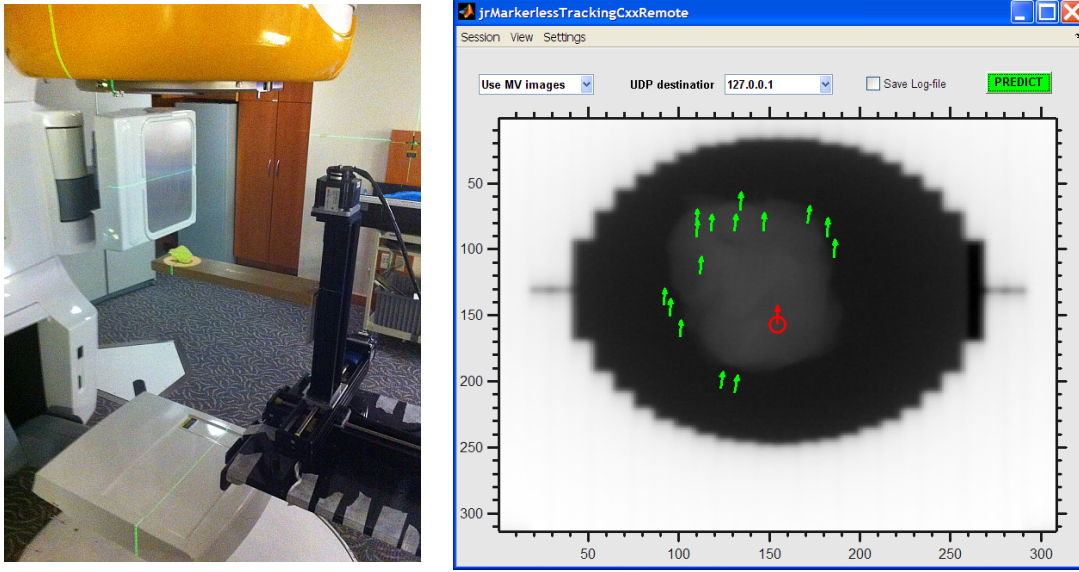
Figure 3.3: *(left)* Setup used for the demonstration experiment with the *Washington University 4D Phantom.* The resin tumor model rests on a solid water slab that is mounted to the motion stages of the phantom. The treatment field light is on to show the outline of the radiation field. The tumor modeled is centered in this field for initialization. *(right)* *Graphical user interface* (GUI) for real-time visual feedback during tracking operation. Each green arrow corresponds to a landmark, the red arrow to the average landmark position (which is fed to the predictor). The window/level of the image was adjusted to let enhance the display contrast for the tumor model.

aperture. The target position is already known and we define the MLC position to be the geometric center of the aperture opening. To calculate aperture position in an automated fashion, a simple segmentation algorithm is employed. Since the gray value gradient $\nabla I(x, y)$ is commonly much larger at the edge of the treatment aperture than anywhere inside the aperture, a gray value gradient based edge detector (*canny filter*[10]) is used to find the rim of the treatment aperture. A typical resulting binary image is shown in Figure 3.4. Because the collimator leafs adjacent to the aperture cannot be completely closed for technical reasons, the resulting gray value gradient introduces artifacts not belonging to the treatment aperture in the canny edge. To remove this effect the original image is pre-processed with a 2d gaussian filter and the binary edge image is further processed with a labeling algorithm that allows to find 4-connected regions. The remaining rim between outside aperture region and inside aperture region does not contain artifacts and its pixels are used as treatment aperture delimiters (see
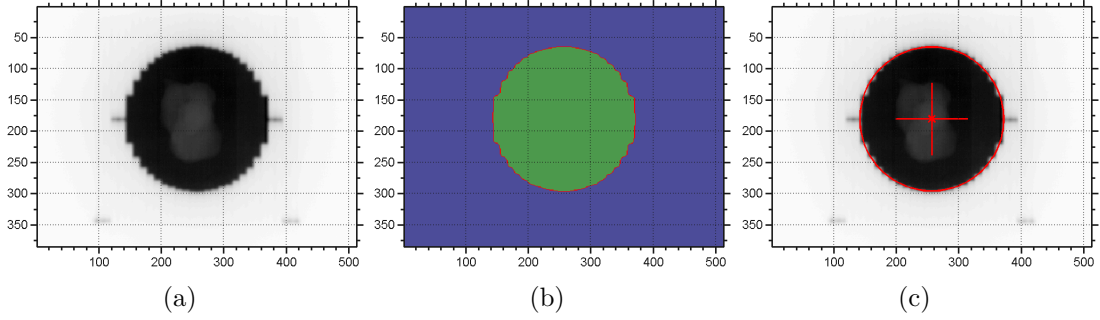
Figure 3.4: Automated calculation of the treatment aperture centroid position. On the *(left)* the input image with tumor model and circular treatment aperture visible is shown. The position of the treatment aperture is calculated by first finding the outline of the aperture with the help of an edge detector (*canny filter*), then finding 4-connected regions in the resulting binary image *(middle)*, getting rid of any artifacts from the edge detection. If the aperture is circular, a Taubin-fit is made to the aperture rim pixels to get center position and radius. The input image with overplayed Taubin-fit is shown on the *(right)*.

Figure 3.4(b)).

For circular apertures, the center of the treatment aperture can then be easily calculated from a *Taubin fit* to the previously calculated treatment field edge pixels. If the treatment aperture has a more complicated shape or is not known up front, the aperture position can be determined as the center of the smallest rectangular box wrapping around the aperture rim. All steps of this procedure are demonstrated in Figure 3.4 including the circular fit.

3.3.1   System latency analysis

The geometric accuracy improvement from incorporating a prediction algorithm depends on adequate training data. The quality of the training data relies on the number of data samples available for training, how well the training data represents the motion to be predicted and how accurately the look-ahead time τ matches the system latency δt_s.

To determine the look-ahead time, the system latency is measured using the setup sketched in Figure 3.2 without the predictor. The aforementioned dynamic phantom is employed to drive a sinusoidal motion with a cycle time of $T = 4.5s$

and a peak-to-peak amplitude of $A = 20\,mm$ in the superior-inferior direction, i.e. in the leaf-motion direction. With respect to motion range and cycle time this scenario is a sufficiently realistic simulation of respiratory motion observed clinically during radiotherapy delivery. Running the system without a prediction algorithm in place results in a shift between target position and aperture position of the MV beam. Calculating the phase shift $\Delta\phi$ between a sinusoidal fit to the target positions $p_{gtv}(t_i)$ and a sinusoidal fit to the treatment aperture position $p_{mlc}(t_i)$ yields the system latency:

$$\delta t_s = T \cdot \frac{\Delta\phi}{2\pi} \qquad (3.1)$$

Results

The results of the system latency measurement for our experimental implementation is shown in Figure 3.5 on the left side for an image acquisition frequency of 12.86 Hz (and motion parallel to the MLC leafs). This setup yielded a system latency of $\delta t_s = 220 - 230\,ms$. The fluctuation occurred on the same treatment machine but with several hours between measurements. The fluctuations are most likely caused by the processor and RAM load level of the tracking computer (cp. Figure 3.2).
For the measurement a constant time delay between the point of image acquisition and the mlc-leafs reaching their requested position is assumed. However, as can be seen from the histogram on the right side of Figure 3.5, depicting the time needed for image acquisition, this is not the case. The variation in the latencies introduces uncertainties that may not be mitigated with a prediction algorithm, since the predictor operates with a constant look-ahead time τ determined by the system latency δt_s.

3.4   Prediction of Breathing Motion

For any system attempting to compensate tumor motion by image guided target tracking there is an inherent implementation specific time interval that is needed for the process of image acquisition, position calculation and hardware adjustment. In the context of dynamic aperture adaptation we define the system latency δt_s to be the time interval needed for the aperture position to reach a given target position. The aperture will therefore reach the target position $p(t_i)$ calculated from an image acquired at time t_i, at time $t = t_i + \delta t_s$ introducing a
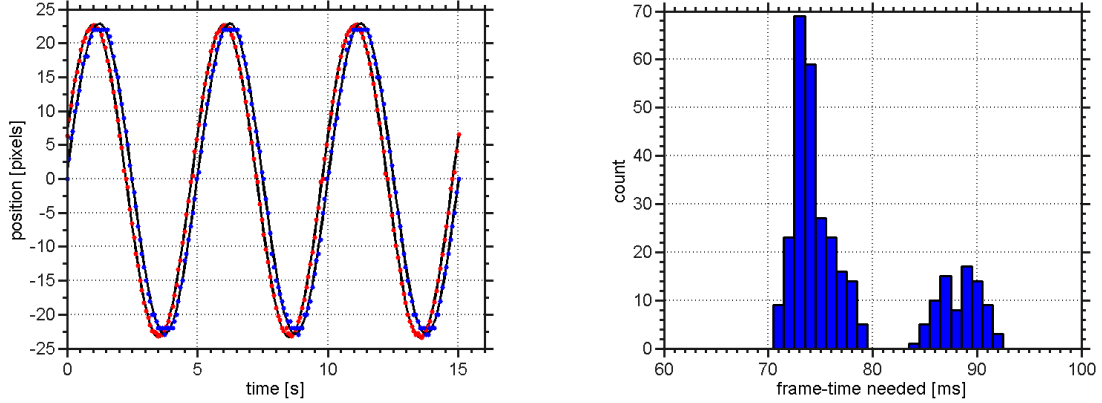
Figure 3.5: Measurement of system latency at a frame of 12.86 Hz with a dynamic phantom driving a sinusoidal motion in the inferior-superior direction. The motion range was set to 20 mm and the breathing cycle period to $T = 4.5s$. **(left)** Sinusoidal fits to tumor position (red) and aperture position (blue). The system latency is determined by the phase shift and the frame rate. We measured values of $\delta t = 220 - 230\ ms$. **(right)** Histogram of the image acquisition timing. The second peak at 90 ms most likely comes from internal memory management.

geometric error. The magnitude of this error naturally depends on δt_s and the target velocity.

As a measure of the average geometric error over the course of a treatment delivery, the root mean square deviation (RMSE) is employed:

$$RMSE = \sqrt{\frac{1}{N} \cdot \sum_{i=1}^{N} \left(\ p_{mlc}(t_i) - p_{gtv}(t_i)\ \right)^2} \tag{3.2}$$

Here $p_{mlc}(t_i)$ and $p_{gtv}(t_i)$ are the treatment aperture and the target position at time t_i, respectively. N is the number of sample points in the motion trajectory examined.

Latency induced geometric error estimation with patient data

To get an estimate for the system latency induced geometric error separately from any other error contributions, we perform a simulation with a set of 3D lung tumor traces. These trajectories were recorded with a commercial fluoroscopic real-time tumor tracking system *(Mitsubishi Electronics Co. Ltd., Japan)* that utilizes orthogonal x-ray tubes to locate fiducial implants during long SBRT treatments (Shirato et al. [62]). The dataset consists of 172 traces sampled at 30 Hz that

(a)

(b)   (c)
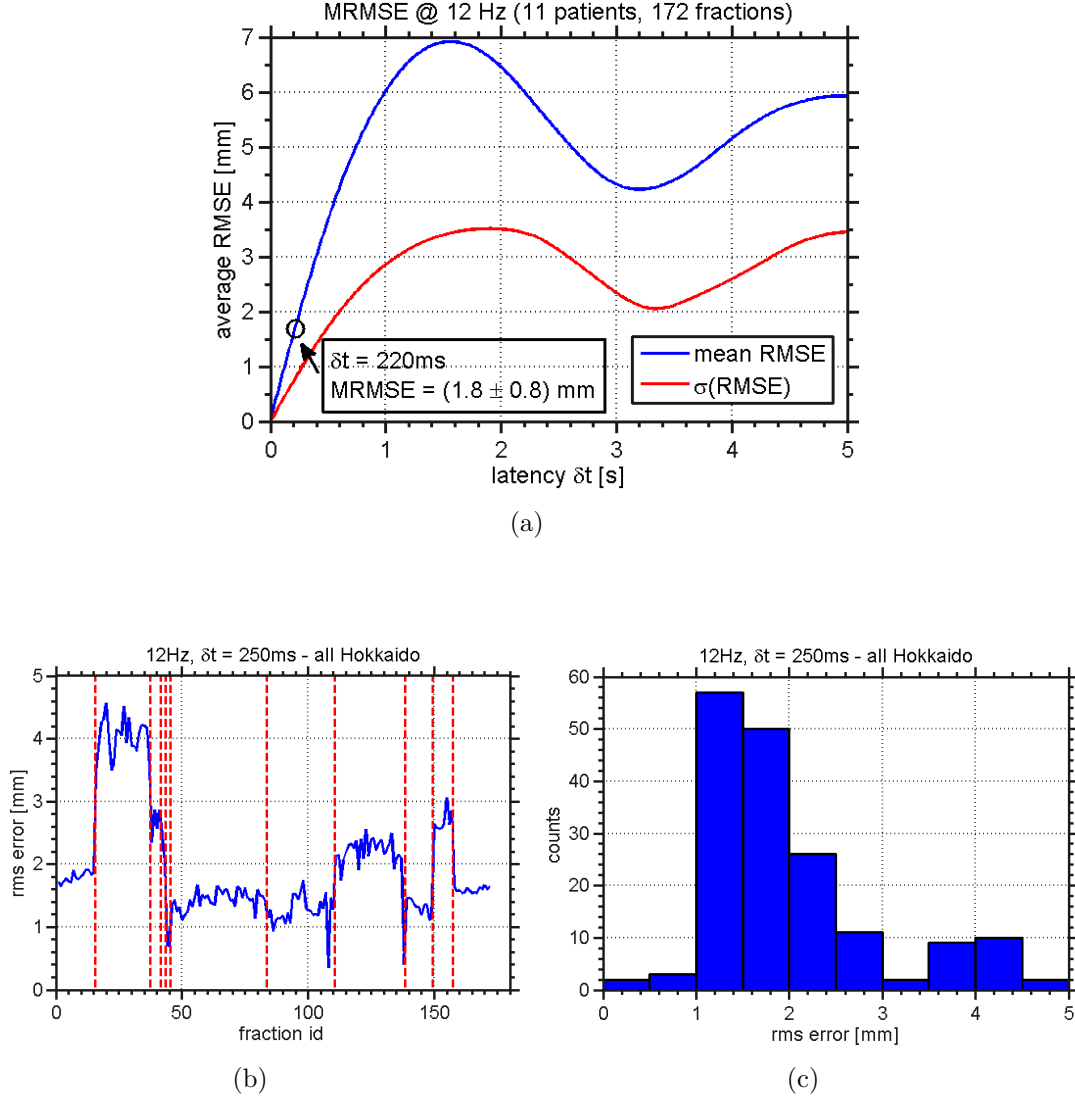
Figure 3.6: Quantification of RMSE contribution from system latency by a simulation based on 172 breathing traces from 11 patients during radiotherapy delivery. The imaging frequency is chosen to be 12 Hz. *(a)* shows the mean RMSE of all traces versus system latency δt_s. *(b)* shows the RMSE for each trace individually; the red bars mark which traces belong to one patient. *(c)* shows for $\delta t_s = 250$ ms a histogram of the RMSE from all 172 traces.

stem from 11 patients treated for non-small cell lung cancer (NSCLC).
A time delay δt_s is introduced to generate treatment aperture positions

$$p_{mlc}(t_i) = p_{gtv}(t_i + \delta t_s), \quad i = 1, \ldots, N \tag{3.3}$$

from the recorded target positions $p_{gtv}(t_i)$ by (linear) interpolation. Figure 3.6(a) shows the latency induced geometric root mean square error (RMSE) as a function of the total system latency δt_s. As an example, the shortest latency time achieved in our experiments (cp. Section 3.3) is $\delta t_s = 221$ ms and results in an error of $RMSE = (1.8 \pm 0.8)$ mm. By comparing to the STiL performance with $RMSE = (0.8 \pm 0.2)$ mm (cp. Section 2.3.1), this demonstrates potential significance of latency with respect to fidelity.

However, whereas geometric errors in the target localization may be difficult to reduce without improved imaging hardware, latency may be overcome through the implementation of prediction algorithms.

Implementation of a prediction algorithm

To reduce the latency induced geometric error, we need to estimate for each target position $p(t_i)$ a future target position $\hat{p}(t_i + \tau_p)$. The underlying assumption in finding this estimate is that the target location at time $(t_i + \tau_p)$ may be expressed as a function of the N_p previous target positions $\{p(t_j) \mid j = (i - N_p), \ldots, i\}$, i.e. we need to define an adequate prediction function

$$f_p \; : \; \left(\, p(t_{i-N_p}), \ldots, p(t_i) \, \right)^T \; \longmapsto \; \hat{p}(t_i + \tau_p) \tag{3.4}$$

Several techniques for constructing f_p have been proposed and compared in the literature: Sharp et al. [61] compared *linear prediction* (LP) with an *artificial neural network* (ANN) and a *Kalman filter* (KF) using patient data traces as simulation input. Considering imaging frequencies of 1-30 Hz and latencies from 33-1000 ms they found ANN and LP to give similar results and consistently outperform KF. Ernst and Schweikard [16] proposed the use of *support vector regression* (SVR) and Ruan [57] proposed a *kernel density* (KD) based prediction algorithm. Krauss et al. [36] implemented and compared LR, ANN, SVR and KD including extensive model parameter optimization on the same dataset from Hokkaido mentioned before. They found the ANN algorithm to work best, closely followed by SVR and LR and all algorithms performing far better than KD.

Comparing the complexities of the algorithms, we have found linear (ridge) regression to be a rather fast and simple, yet still appropriate method for construction of f_p (cp. Krauss et al. [36]). In this case the prediction function f_p can be explicitly written as

$$f_p(\boldsymbol{x_i}) = \alpha^T \boldsymbol{x_i} + \alpha_0 \tag{3.5}$$

if we define $\boldsymbol{x_i} := \left(p(t_{i-N_p}), \ldots, p(t_i) \right)$. For practical purposes the constant term α_0 can be omitted if we pre-process all input data to have a mean value of zero. Additionally we can neglect any kind of scaling differences between training data and testing data[2] if all input data is normalized to have a standard deviation of unity. The transformation is applied to each position $p(t_i)$ in the form of a sliding window operation using the N_p previous positions to calculate the standard deviation σ_i and the mean value m_i

$$\tilde{p}(t_i) = \frac{p(t_i) - m_i}{\sigma_i} \tag{3.6}$$

if we use

$$m_i = \sum_{k=i-N_p}^{i} \frac{p(t_k)}{N_p} \qquad \sigma_i = \sqrt{\frac{1}{(N_p - 1)} \sum_{k=i-N_p}^{i} (p(t_k) - m_i)^2} \tag{3.7}$$

Considering a set of N_t value pairs of training data: $\{(\tilde{\boldsymbol{x}}_i, \tilde{y}_i) \mid i = 1, \ldots, N_t\}$ with normalized predicted positions $\tilde{y}_i = \tilde{p}(t_i + \tau)$ that may be calculated by linear interpolation, the weight vector α can be written as an analytic expression:

$$\alpha = (X^T X + \lambda \mathbb{1})^{-1} X^T Y \tag{3.8}$$

Here $X = (\tilde{\boldsymbol{x}}_1, \ldots, \tilde{\boldsymbol{x}}_{N_t})^T \in (\mathbb{R}^{N_t} \times \mathbb{R}^{N_p})$ is a matrix containing in each row a training vector $\boldsymbol{x_i}$, $Y = \left(\tilde{y}_1, \ldots, \tilde{y}_{N_p} \right)^T$ is a column vector containing the interpolated target positions at times $(t_i + \tau)$ and λ is the Tikhonov regularization parameter, which helps to keep the matrix inversion also for the cases of a poorly conditioned X numerically stable. There is one free model parameter (λ) which can be freely chosen. Krauss et al. [36] have found that a patient independent tuning of prediction model parameters is generally adequate, so we follow this approach and tune this parameter with traces that are not later used for prediction.

---

[2]This is particularly convenient if other sources of input are used in a complementary way as for instance external surrogate data for training the model.
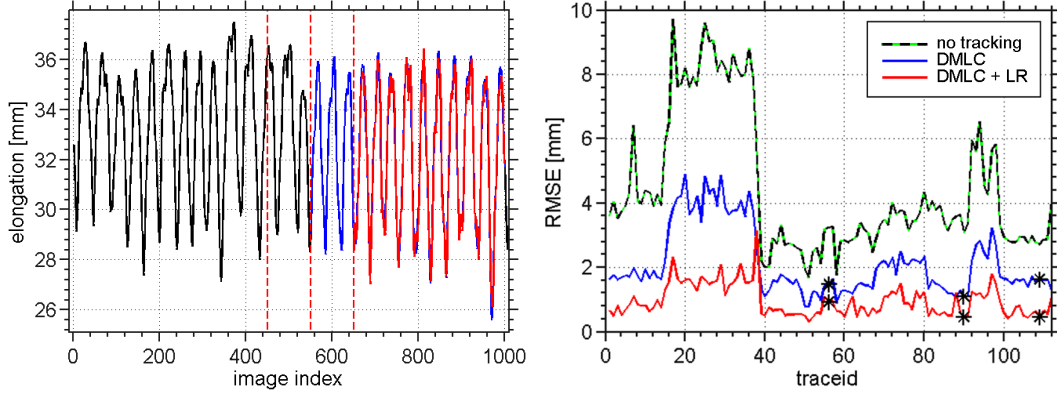
Figure 3.7: Linear predictor performance on uniformly sampled patient data traces (recorded from lung SBRT deliveries). *(left)* A sample tumor trajectory (superior-inferior direction). The marked areas are from left to right: training data used to build the model, waiting data (to allow for model calculation), training data to train the model and finally application of the predictor. During the last section the red line is the predicted curve shifted by the expected system latency δt_s. Therefore perfect overlay with the blue curve would mean RMSE = 0. *(right)* The resulting root-mean-square (RMSE) error during the prediction period: without any tracking (black/green), with tracking but without prediction (blue) and with tracking and prediction based on models trained with internal tumor motion data. The black stars mark the traces that were later delivered to a dynamic phantom.

Estimated predictor performance on uniformly sampled motion traces

To estimate the geometric prediction error without any influence from other sources of uncertainty, e.g. the measurement of the target positions $p(t_i)$, the aforementioned prediction algorithm was tested with patient tumor trajectories taken as ground truth. From the original 172 traces, 114 traces were selected. The sole selection criterion was to have ≥ 1015 sample points available. Each trace was then divided into a training data set of length N_t, a waiting time of length N_{wait} sample points giving sufficient time to calculate the model and the actual test data set of length N_{test} samples during which the predictor model is first trained for N_p samples and then applied to the remaining sample points. The following table gives an overview of the parameters used:
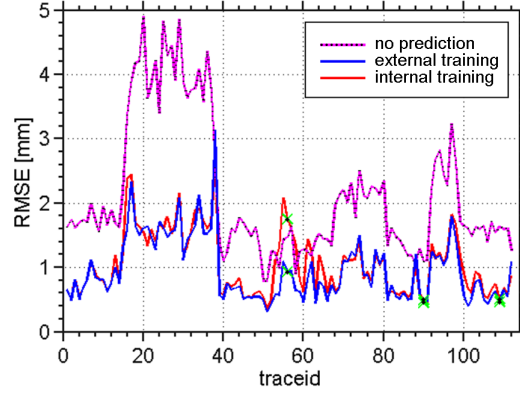
Figure 3.8: A comparison for using internal tumor motion data versus external surrogate motion data to build a linear prediction model. The RMSE for training with internal data is depicted in blue and for training with external surrogate data in red. The RMSE for not using any prediction at all is shown in pink for comparison. The green/black stars denote the three trajectories used for the physical phantom study.

parameter	frame rate	$\tau = \delta t_s$	λ	N_p	N_t	N_{wait}	N_{test}
value	12.86 Hz	250 ms	0.025	100	450	100	450

A sample tumor motion trace is shown in Figure 3.7 on the left and the resulting RMSE for all examined traces is depicted on the right. The time needed to calculate the linear prediction model was < 150ms for all traces and (52 ± 11)ms on average, i.e. a waiting time of $N_{wait} = 3$ would be already sufficient in this scenario to calculate the model.

It is apparent from Figure 3.7 that linear prediction can generally reduce the geometric error introduced by a well defined system latency.

Training with an external surrogate

Using the therapy beam to acquire the data required for the prediction model calculation may be inconvenient in clinical operation: with parameters chosen for this study about 35 s beam-on time would be necessary. An approach to get around this problem may therefore be to calculate the model not from EPID images but from external surrogate data. To investigate this option the complementary external surrogate data of the lung tumor trajectory data set was utilized instead of the tumor position for training the model - everything else was

kept as in the previous section. The result is depicted in Figure 3.7 as the dashed pink line. While the performance is patient dependent, overall, training with an external surrogates gives similar results as training with the internal target position. Therefore it may be worthwhile to consider this option where direct tumor motion data for model building is not available.

3.5 Geometric accuracy with realistic phantom data

To quantify the geometric accuracy of the integrated tracking system as depicted in Figure 3.2 three lung tumor traces were selected by longest duration, largest motion range and most irregular motion pattern. The superior-inferior motion direction of each trace was loaded to the 4D motion phantom and a radiation beam with a circular aperture covering the lung tumor phantom was delivered. A photograph of the setup in the treatment room is shown in Figure 3.2. The predictor model was trained in a separate session before with the predictor look-ahead time set equal to the previously measured system latency ($\tau = \delta t_s$ on that day). The other predictor parameters were chosen to be the same as listed in Section 3.4. Also, the STiL algorithm was initialized ahead of the start of the phantom to avoid too fast motion requests for the treatment aperture, potentially triggering a beam hold, once the initialization is finished. The unreasonably fast motion requests are due to the serial implementation of the STiL algorithm[3], i.e. the frame processing is blocked until the initialization is completed and then catches up as fast as the operating computer permits.
A time buffer of 100 frames is given after the phantom motion is started for the aperture to synchronize with the target motion. Thereafter the model is trained for $N_p = 100$ frames before prediction is started.

Results

The three sample traces investigated in this study are shown in Figure 3.9 with their respective error histograms. The STiL algorithm operates in real-time and provides target positions to the predictor that allow the treatment aperture to follow the target motion in real-time keeping the aperture statically centered on the target. The error histogram also clearly shows a shifts towards smaller errors

---

[3]Matlab® does not permit multi-threading in the version we used (2008a).
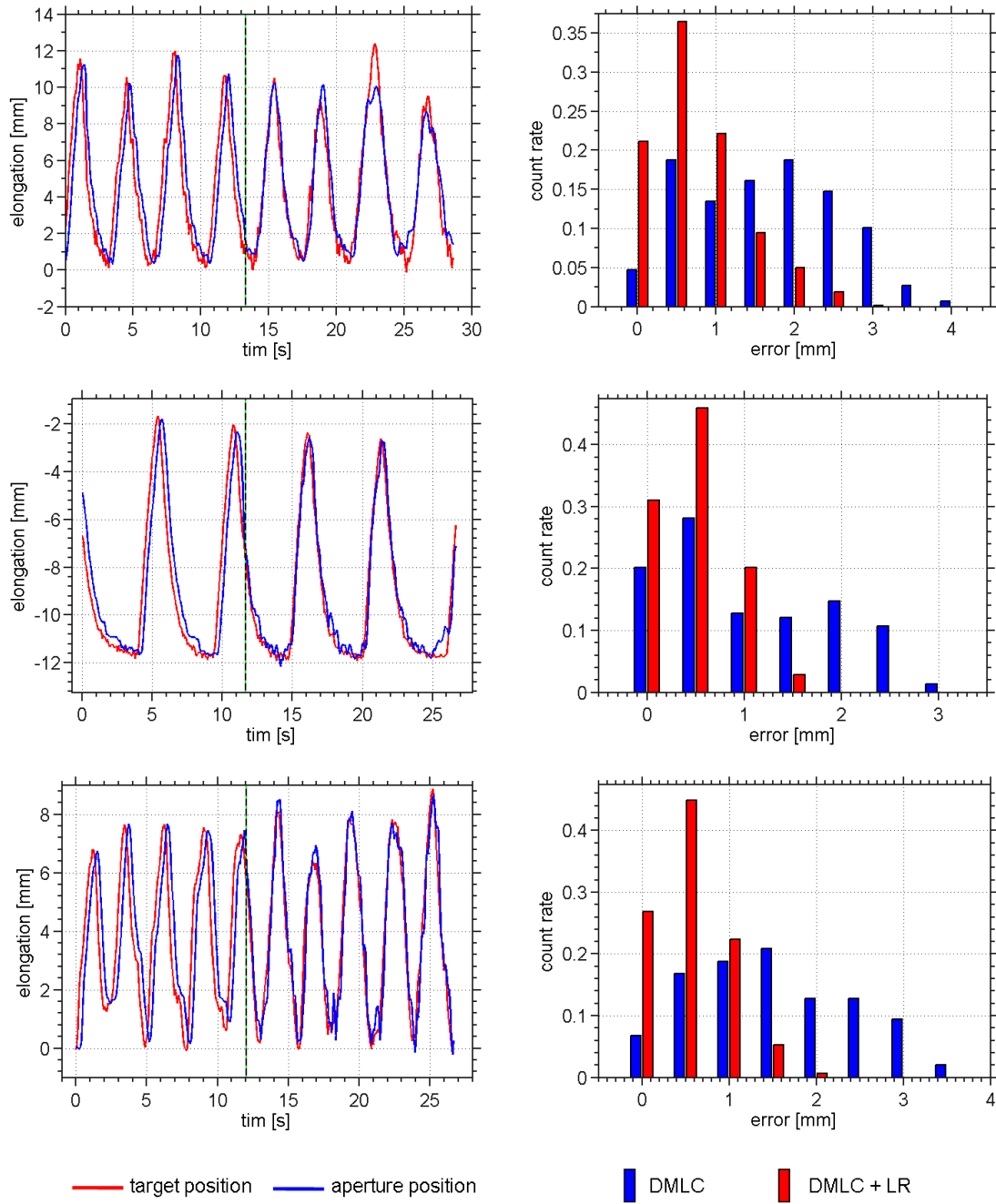
Figure 3.9: Experimental results of the physical phantom study. Each row refers to the delivery of one lung tumor trace. The RMSE from top to bottom are before $\longrightarrow$ prediction starts: $1.9\,mm \longrightarrow 0.9\,mm$ (top), $1.4\,mm \longrightarrow 0.6\,mm$ (middle), $1.8\,mm \longrightarrow 0.7\,mm$ (bottom) **(left column)** The target position (red) and the aperture position (blue) are plotted over time. The black/green dotted line denotes the start of prediction. **(right column)** Error histograms for each trace before prediction is in place (blue) and after (red). The histogram is normalized to unity integral counts.

once the predictor has started operation. The results are summarized in the table below:

trace	static beam RMSE [mm]	DMLC RMSE [mm]	DMLC + LR RMSE [mm]	static beam ↓ DMLC	static beam ↓ DMLC + LR
1	3.4 ± 3.8	1.9 ± 1.9	0.9 ± 0.9	55 %	27 %
2	3.2 ± 3.2	1.4 ± 1.4	0.6 ± 0.6	43 %	19 %
3	2.4 ± 2.4	1.8 ± 1.8	0.7 ± 0.7	74 %	29 %

For the investigated traces it is shown that DMLC tracking with a linear predictior can significantly reduce the residual tumor motion.

3.6 Summary and discussion

In this chapter we have consecutively stepped through the building blocks of a real-time DMLC tracking system based on soft tissue localization from cine MV-EPID images and demonstrated its performance on a physical dynamic phantom.

As a prerequisite, the expected system latency (δt_s) induced geometric (root-mean-square) error of a perfect[4] DMLC tracking system was calculated as a function of δt_s in a simulation study based on a set of 172 lung tumor trajectories recorded from lung SBRT deliveries. Plotting the RMSE over δt_s shows a sharp increase of RMSE for small latencies. It is therefore advisable to keep the system latency at a minimum e.g. through fast image acquisition and a high frame. The frame rate reduces the system latency because the motion requests to the MLC leafs are for smaller distances. For the system latency of our experimental setup (see below, $\delta t_s = 220 \ ms$), we calculated an expected average RMSE of $(1.8 \pm 0.8) \ mm$.

In order to mitigate the residual system latency induced geometric error, a linear prediction algorithm was implemented. It's performance for our specific system latency is simulated on the same lung tumor motion trajectories. The prediction algorithm is found to reduce the residual geometric error in all 112 trajectories

---

[4]Perfect in the sense that a fixed system latency but no uncertainties from position measurement or leaf-motion assumed.

investigated and is therefore considered appropriate for the purpose of system latency induced geometric error mitigation.

A physical implementation of the system was conducted by integrating a frame grabber for fast image acquisition, the STiL algorithm for real-time target localization, the linear predictor and a DMLC tracking(Sawant et al. [58]).
The system latency was measured (without linear prediction) using a dynamic motion phantom driving a realistic lung tumor model on a sinusoidal motion trajectory. The trajectory parameters were chosen to resemble human respiration (20 mm peak-to-peak, $T = 4.5$ s) and the motion was directed in the superior-inferior direction, in parallel to the MLC leafs. Radiation with a circular treatment aperture was delivered to the phantom and the phantom motion extracted from cine EPID images with the STiL algorithm was tracked with the therapy beam aperture in real-time. A system latency of $\delta t_s = 220 - 230$ ms was observed. We attribute the fluctuation in δt_s to CPU and RAM load fluctuations of the tracking computer.

The motion compensation abilities of the integrated tracking system were experimentally characterized with the same setup used for the latency measurement. Instead of a generic sinusoidal motion trajectory, lung tumor trajectories recorded from patients during SBRT deliveries were used. The motion was directed in the superior-inferior direction and parallel to the MLC leafs.
DMLC tracking was found to reduce the residual geometric error introduced by intrafractional tumor motion by more than 42% on average in this dynamic phantom study. The integration of a linear predictor in order to mitigate the geometric error induced by the system latency of $t_s = 220$ ms can reduce the residual geometric error to below 1 mm.

Outlook: Dynamic aperture shrinking

Shrinking the treatment aperture once tracking has been established can potentially open the door to a significant reduction of normal tissue toxicities and/or further radiation dose escalation. A qualitative retrospective simulation study (Rottmann et al. [55]) utilizing MV-EPID images acquired from patients undergoing lung SBRT treatment for NSCLC was undertaken. To overcome the slow sampling rate of 2 Hz, the adjustment of the aperture position was performed with the position estimate on the same image. The feasibility of the aperture
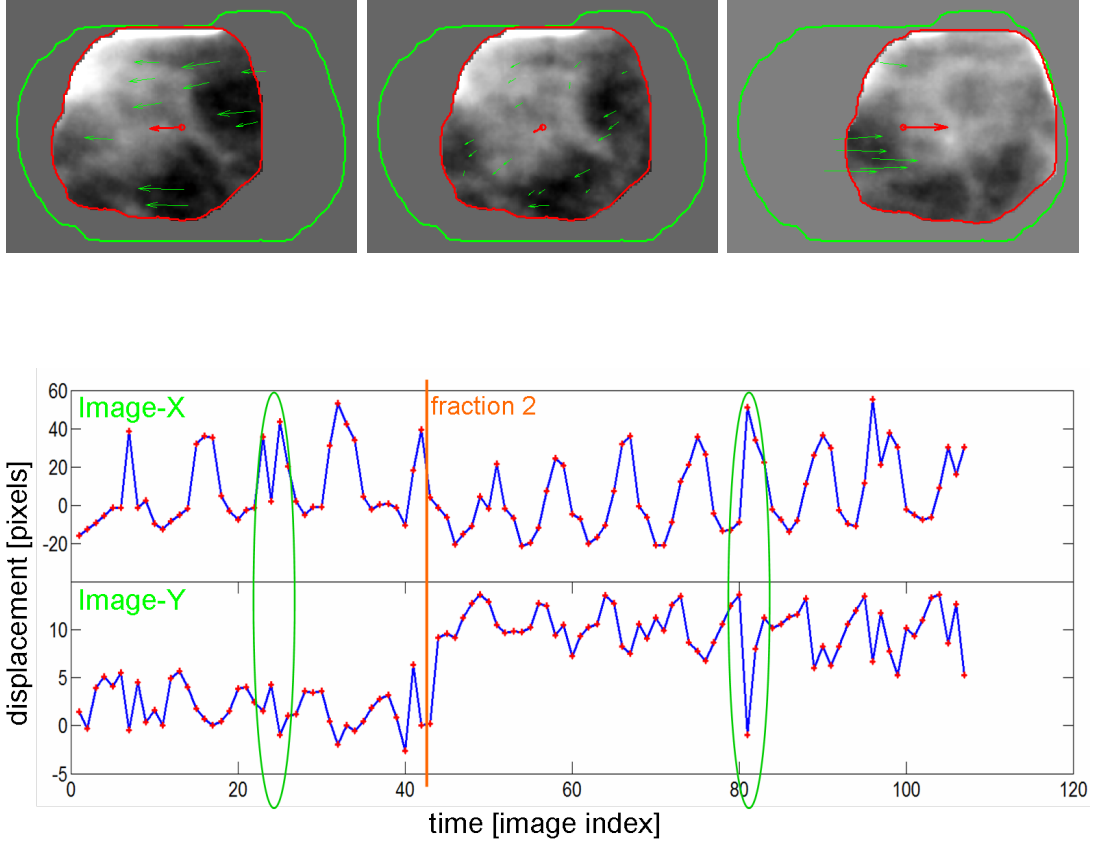
Figure 3.10: Simulation of aperture shrinkage during 3D conformal radiotherapy delivery. *(top)* MV-EPID images were acquired during a lung SBRT delivery at a sampling rate of 2 Hz with a Varian AS-1000 EPID. Only the pixels within the GTV (contoured in red) were used to estimate the GTV position on the next image (no prediction algorithm was used). The green arrows mark the displacements of the individual landmarks, the red arrows the average displacement. *(bottom)* Trajectory of tracking with the simulated shrunk treatment aperture from above ($\approx 50\%$ of the original (PTV) aperture area contoured in green). The aperture is moved to the concurrently tracked position (rather than to the next one) to overcome the long latency introduced from the low sampling rate (2 fps). For the two positions marked in green tracking failed and the margin would need to be increased back to PTV margins.

shrinking concept utilizing the STiL algorithm was investigated qualitatively. The bottom row of Figure 3.10 shows the resulting motion trajectory. Only for the points circled in green tracking failed.

It should be pointed out that the presented strategy does not impose more over-dosage risk to the patient than a regular treatment with the full aperture since the motion of the GTV aperture is restricted to within the PTV area. Also, as soon as a tracking failure would be detected, the field would be opened up back to the PTV size.

However, the low sampling rate of 2 fps somewhat limited the ability to draw conclusions for a realistic clinical scenario. So, further study will be required to confirm the initial findings on imagery acquired with a higher frame rate and to investigate efficient methods for failure detection and mitigation. Figure 3.10 shows EPID images from the simulation illustrating the concept.

3.7   Conclusions

We have demonstrated in a physical phantom study that using a soft tissue lo-calization (STiL) algorithm to drive real-time beam aperture adaptation during radiation delivery is feasible. Using the MV-EPID for image acquisition and a markerless STiL algorithm to estimate tumor motion is an advantage when com-pared to other systems that utilize an *on board imager* (OBI) with implanted fiducial markers. Our approach neither adds any additional dose nor does it expose the patient to the risk of pneumothorax from the marker implantation procedure.

The inherent system latencies induce a geometrical error, i.e. a lag between tumor and treatment aperture position. We demonstrate that the magnitude of this error can be efficiently reduced by employing a simple linear prediction algorithm. We also show that the model for this algorithm can be derived from internal (tumor position) as well as from external (surrogate) training data.

4 Delivered dose calculation with STiL

In this chapter a simple method for delivered dose calculation with the MV EPID is presented. Section 4.1 motivates the calculation of delivered dose in general and in particular using the electronic portal imaging device and the treatment planning system. In Section 4.2, a method based on 2D tumor trajectories generated with the STiL algorithm (cp. Chapter 2) is proposed. The method is demonstrated with a simple application to both phantom data and patient data in Section 4.3. A summary and conclusions are given in Section 4.4.

4.1 Motivation: delivered dose vs planned dose

The clinically delivered dose may differ from the planned dose in external beam radiotherapy. This is mainly due to setup uncertainties, interfractional changes of patient anatomy (e.g. from tumor shrinkage due to the radiation exposure) or intrafractional organ motion due to respiration, heart beat or bowel movement (depending on the treatment site). These effects are well known and taken into account during treatment planning by assigning enlarged treatment margins. It is generally assumed that this strategy provides sufficient dose coverage to establish local control. If the treatment consists of about 30 fractions, randomly distributed errors in the positioning of the patient on the treatment table (setup error) may average and the effects of a very poor setup during one fraction are less likely to compromise the treatment outcome. However, hypofractionated treatments with only 3-5 fractions are more sensitive to uncertainties because the dose per fraction is much higher and margins are usually kept small to minimize normal tissue toxicity. In this context techniques for the calculation of delivered dose are highly desirable.

Accurate dose calculation requires knowledge of the patient's electron density distribution throughout the treatment. However, continuous volumetric imaging is not (yet) clinically available. Therefore some assumptions are necessary to

address the problem with currently available equipment.

The most straight-forward approach is to use already available volumetric CT data, which may include a 4DCT data set taken a few weeks before treatment and daily 3D or 4D CBCT's that are often used for patient setup and treatment verification before and after fraction delivery. For each voxel, a displacement vector can be calculated with the help of deformable image registration algorithms, resulting in a deformation vector field (DVF) that maps each voxel from the various CT's to the planning CT used for dose calculation. This approach is for example followed by Flampouri et al. [18]. This technique is suitable to capture interfractional changes of the setup and patient anatomy. Intrafractional motion however, cannot be directly resolved in this approach and is modeled from the motion patterns seen during imaging sessions rather than during treatment delivery. For targets within the lung, respiratory motion is a major source of uncertainty with respect to both accurate setup to a moving target and intrafractional motion. To accurately describe respiration on a voxel grid, the DVF has to become time dependent, i.e. we need to find for each voxel a displacement trajectory $\text{DVF}_{i,j,k}(t)$ that describes its motion and deformation throughout the treatment delivery.

The only (currently) available image data during treatment delivery are kV-fluoroscopy and MV-EPID images. While kV-fluroscopy has excellent contrast and resolution, the portal imager captures the exit dose without adding any additional patient dose (Kilby and Savage [33]). There have been several studies utilizing the EPID: Nijsten et al. [45] compare the the central field dose back-projected to a certain water equivalent depth with the planned dose taking the dose discrepancy as an indicator for in-treatment errors. McDermott et al. [41] and Louwe et al. [40] use the EPID information in combination with CBCT to reconstruct 3D dose distributions.

However, all of the above studies do not utilize the tumor motion information directly for dose calculation but rely on pre-treatment imaging alone for this part. We therefore follow an approach that explicitly incorporates the target motion into the delivered dose calculation.

4.2 EPID based delivered dose calculation

We monitor the treatment delivery with continuous MV-EPID imaging and retrospectively calculate the target position throughout the treatment.
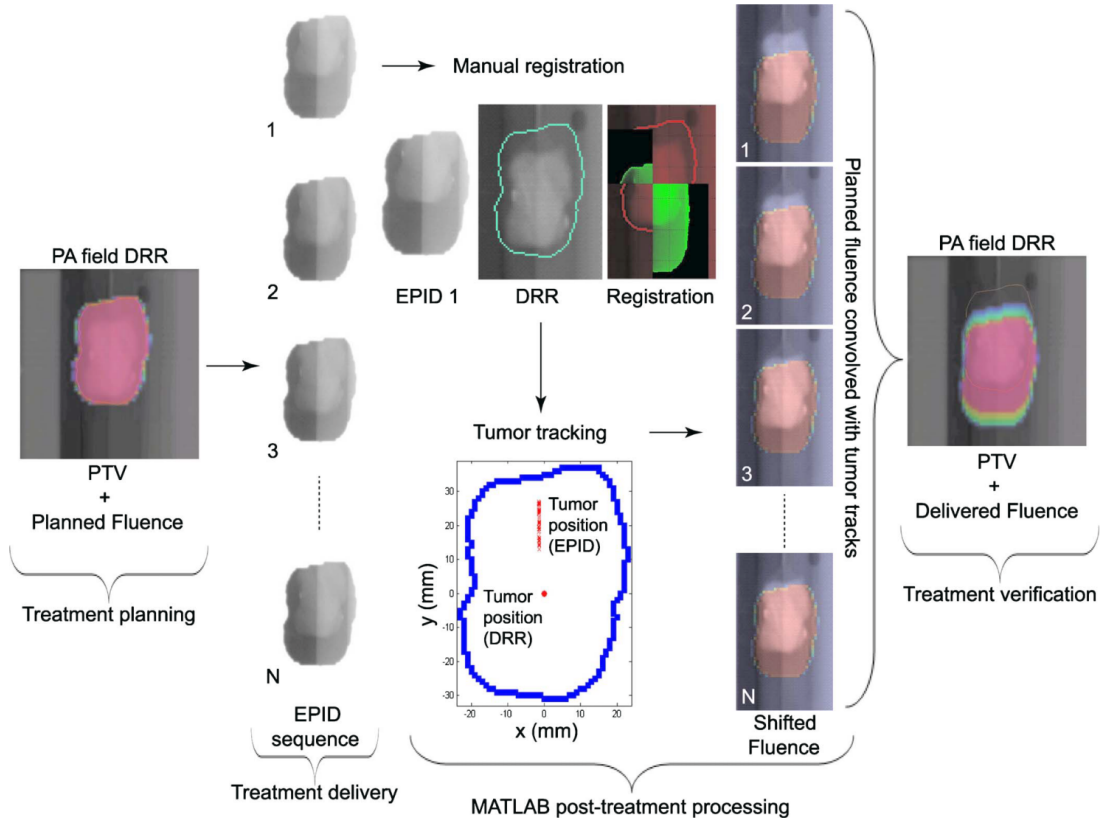
Figure 4.1: Workflow of the 3D dose calculation procedure. The time flows from left to right: treatment planning, delivery with EPID acquisition, linking the planning CT coordinate system to the EPID coordinate system by manual registration, calculation of tumor motion with the STiL algorithm, fluence convolution (cp. Eq. (4.1)) and dose calculation with the treatment planning system.
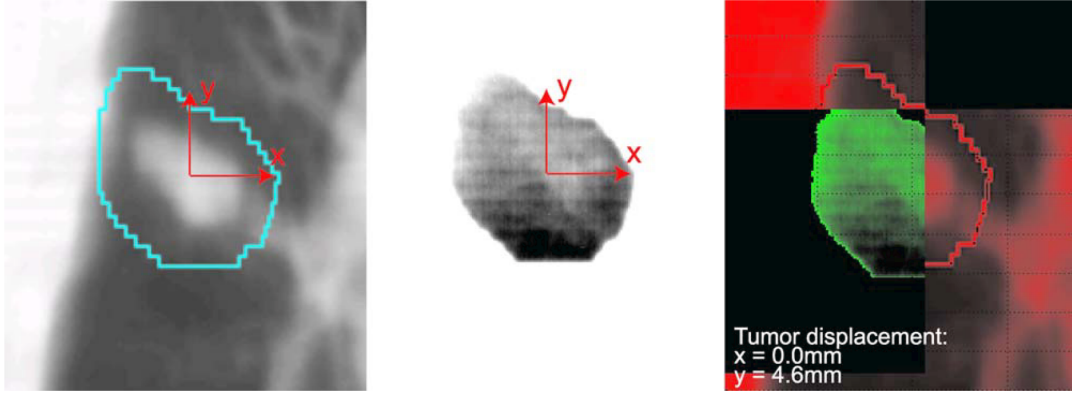
Figure 4.2: Manual registration of the EPID sequence to the planning CT. On the *(left)* a digitally reconstructed radiograph (DRR) of the patient is shown. In the *(middle)* a sample EPID image of the same treatment field is shown. On the *(right)* the registration tool is shown. The tool was kept quite similar to the tools used in the clinic: it allows translational movement of an image to be registered (green) over the reference image (red). Each beam/fraction sequence of EPID images was registered to the planning CT in this way.

To simplify the situation, we assume the target to be static within the patient. Then target motion can be described as a rigid body transformation of the whole patient and delivered dose can be calculated by simply shifting the patient CT images according to tumor motion. Considering only co-planar beam geometries, tumor motion in the beam direction can be regarded as negligible compared to motion in the plane perpendicular to the radiation beam. Additionally, tumor motion parallel to the radiation beam is dosimetrically less important because of the shallow depth dose falloff for photon beams (see Figure 2.1). In conclusion it may be sufficient to use only two dimensional tumor trajectory information from an isocentric plane perpendicular to the radiation beam axis to approximate the 3D tumor motion.

The procedure for calculating delivered dose is the following (cp. Figure 4.1):

i) The treatment is planned as usual and the delivery is monitored with continuous EPID imaging.

ii) The STiL algorithm is used to estimate the tumor trajectory within the isocentric plane perpendicular to the radiation beam at N points $\{\ p_i = p(t_i) \mid i = 1, \ldots, N\ \}$ each corresponding to one portal image. The origin is linked to the planning CT by manual registration of a reference EPID

image I^* to a digitally reconstructed radiograph (DRR) generated with the treatment planning system (TPS) for each treatment field.

iii) The delivered dose is calculated with the clinical treatment planning system (Eclipse by Varian Medical Systems, Palo Alto, USA) using the original planning CT. Instead of performing for each of the N target positions a separate dose calculation and then integrating over the resulting dose distributions, it is significantly less computationally expensive to integrate shifted fluence maps and then calculate the delivered dose in one step. For each beam direction - identified by gantry and couch angle (g, c) - the planned fluence map $\Phi_{g,c} = \Phi_{g,c}(x, y)$ is exported in order to calculate a delivered fluence map. The planned fluence map $\Phi_{g,c}$ is shifted for every time step $\{t_i | i = 1, \dots, N\}$ by the displacement vector $p(t_i) = (p_i^{(x)}, \ p_i^{(y)})^T$. The delivered fluence map is then given by the integral over all partial fluence maps normalized to the number of time steps:

$$\Phi_{g,c}^D(x, y) = \frac{1}{N} \sum_{i=1}^{N} \Phi_{g,c}(x - p_i^x, y - p_i^y) \tag{4.1}$$

The delivered fluence map $\Phi_{g,c}^D(x, y)$ is then imported back into the TPS to calculate the delivered dose.

4.2.1 Verification with a dynamic thorax phantom

To validate the concept, a phantom study was conducted comparing the delivered dose calculated with the proposed method to measurements taken with 15 *metal oxide semiconductor field effect transistors* (MOSFETs)[1] placed inside the target. The goal of this study was to show that the calculated delivered dose exhibits a similar dose drop off for setup errors and/or unexpected changes in motion range that exceed ITV/PTV margin as an actual measurement.

The resin tumor model (already introduced in Section 2.3.1 and described in detail in (Court et al. [12])) was used as the target. For this purpose it was constructed with small fissures to hold the MOSFETS. A picture is shown on the right side of Figure 4.3. All measurements were taken on a Novalis TX clinical linear accelerator with a CIRS dynamic thorax phantom (see left side of Figure 4.3). The CIRS phantom can be programmed to drive the target according to arbitrary

---

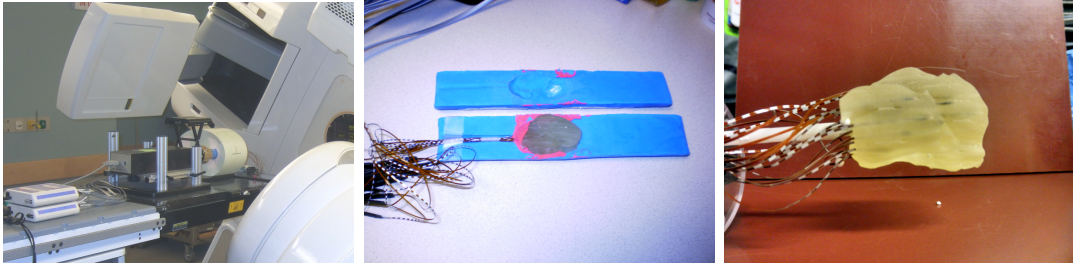[1]Standard MOSFET, Best Medical, Canada

Figure 4.3: Experimental setup for the verification experiment with a CIRS dynamic thorax phantom. On the *(left)* the phantom is depicted on the treatment couch of a Novalis TX treatment machine with the EPID in imaging position in the ground. The MOSFET readout electronics are visible on the left foreground. In the *(middle)* the tumor model embedded in a slab of modeling clay is shown. This lung density inlay was custom fitted for the CIRS phantom. The cables hanging out from the back connect the MOSFETs to the read-out electronics. On the *(right)* a closeup of the resin tumor model is shown. The light stripes are the fissures in the model made for the MOSFET.

superior-inferior motion traces. We chose a patient data trajectory recorded with the Mitsubishi RTRT system in Hokkaido (see Chapter 2) that showed a large superior-inferior tumor motion and set the average peak-to-peak motion range to 15 mm. A planning 4DCT was taken and a 3D conformal treatment plan mimicking a lung SBRT treatment was created using maximum intensity projection to define an ITV and a 5 mm margin surrounding the ITV to define a PTV (cp *(right)* side of Figure 1.3). The plan consisted of 7 coplanar beams ($\phi_c = 0°$). Since the effect of superior-inferior motion is rather small for non-coplanar fields in beams-eye-view (slow photon depth dose curve fall-off), no fields requiring couch rotations were applied. On a static CT, acquired with no target motion, the 15 MOSFETs were contoured as small enclosing volumes. The measured delivered dose can then be defined as the average dose within these small contoured volumes.

To avoid pushing the MOSFETS to their dose collection limit with a single SBRT treatment delivery, the fractional dose was chosen with 200 cGy to be a fraction of a typical lung SBRT case (12-18 Gy). However, to keep the treatment delivery time similar to clinical practice the dose rate was lowered from the clinically typical 600 MU/min to 100MU/min. The treatment duration was then $\approx 25\ s$ of beam-on time per treatment field, which is about average for clinical SBRT

patient treatments.

MOSFETs need to be calibrated for absolute dose readings and there are numerous publications available on this topic [49, 59]. However, to verify that our method can recover motion effects on delivered dose, it is sufficient to calibrate against a static delivery (no tumor motion) of the prepared plan, i.e. for each MOSFET a calibration factor c_i is calculated and applied to the delivered doses calculated with the TPS:

$$D_{\text{TPS}} = c_i \; D_{\text{TPS}}^{raw}$$
$$\text{with} \qquad c_i = \frac{\text{dose measured with MOSFET}}{\text{dose calculated with treatment planning system}} \qquad (4.2)$$

The phantom was set up on the treatment table with orthogonal kV radiographs to match the PTV to the planning CT. The following combinations of artificial setup errors and superior-inferior motion range were chosen:

trial number	1	2	3	4	5
peak-to-peak motion [mm]	0	15	30	15	15
setup error [mm]	0	0	0	10	20

During radiation delivery MV-EPID images were acquired at a frame rate of 3 Hz while the portal imager was set at an imager to source distance of $ISD = 180 \; cm$, resulting in an isocenter pixel spacing of $0.43 \, \text{mm}$.

Results

The results of the verification experiment are shown in Figure 4.4. As expected the measured dose agrees with the calculated dose well for the measure points that stay within the treatment aperture (PTV) at all times. For the measurement points that move partially out of the PTV during radiation delivery both, the measured as well as the calculated delivered dose show a drop off as expected. However, increasing discrepancies can be observed for increasing setup error/motion range. There are several factors contributing to this phenomenon:

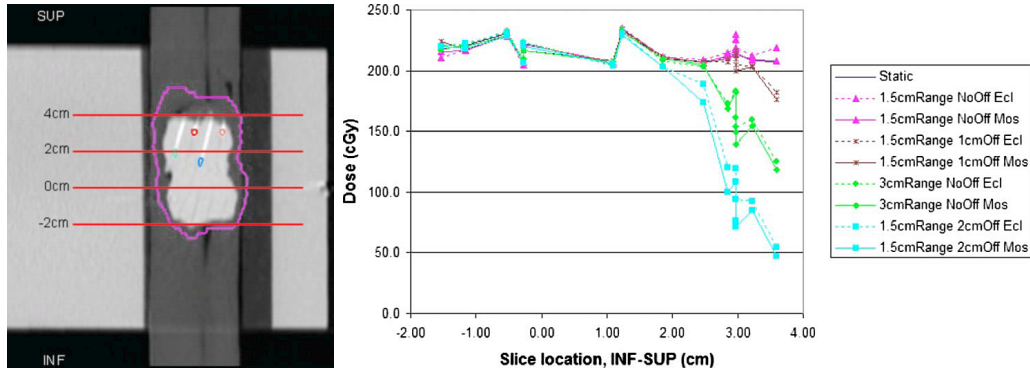(i) The calculated delivered dose is defined as the average over a small volume

Figure 4.4: The *(left)* side shows a coronal plane of the static CT with the PTV contour drawn in pink. There are also four of the MOSFET contours visible in this plane, the white stripes are the fissures containing the wires for the readout. On the *(right)* side the measured and corrected calculated dose are shown for all setup errors and motion ranges.

surrounding the actual point of measurement. Therefore a steep dose gradient in the vicinity of the MOSFET location may show in the average value while it does not in the MOSFET reading.

(ii) The calculated dose is time sampled, i.e. the fluence map is only shifted once every 333 ms, potentially accelerating the previous effect even more.

(iii) For the AAA algorithm, used to calculate the dose in the TPS (Eclipse, Varian Medical Systems), dose deviations have been reported for beams going through the lung (up to 7 % for 6MV photon beams (Robinson [50])).

However, in summary it has been shown with this experiment that the trend of underdosage can be observed with both, measurement and calculation.

4.3   Example for a lung SBRT delivery

To demonstrate the delivered dose calculation method in a realistic scenario, a lung SBRT treatment was monitored with continuous MV-EPID imaging at a frame rate of 2 Hz. To reduce noise in the MV images, each frame was the average of 4 frames, i.e. the raw imaging frequency was 8 Hz. The patient received a total of 60 Gy in 5 fractions to each 12 Gy delivered at 600 MU/min. The prescription called for 90% of the PTV to receive 95% dose. A compression plate was used in order to reduce respiratory target motion (cp. Section 1.4.2).

Field number	Gantry [°]	Couch [°]	images/fraction
01	225	0	41
02	285	0	54
03	315	0	59
04	30	90	36
05	340	90	41
06	30	0	37
07	90	25	44
08	90	335	38
09	160	340	37
10	180	0	36
11	110	0	39

Table 4.1: Parameters for the lung SBRT treatment used for the delivered dose calculation demonstration

A list of the treatment fields and their configuration is given in Tab. 4.1. The "mean-shift" is the mean tumor position relative to the planning CT's tumor position and can be considered as a measure of the setup error. To calculate the mean-shift, a reference EPID image was selected from first fraction for each beam direction; the selection criterion was solely based on maximal image quality (minimal motion blurring). The reference EPID was manually registered to a DRR calculated with the TPS from the planning CT (see Figure 4.2). The *Hounsfield unit* (HU) range as well as the projection volume were clipped to resemble an MV-DRR as close as possible. The tumor trajectory was used to calculate a delivered fluence $\Phi_{g,c}^{D}$ according to Eq. (4.1).

Results

The resulting tumor trajectories are shown in Figure 4.5 for Field-01 (an AP-field) for all fractions as a showcase. They are depicted along with *dose volume histogram* (DVH) plots for the ITV at each treatment day. The DVH for the entire treatment is shown in Figure 4.6.

As expected, the DVH is influenced by the mean-shift position of the tumor:
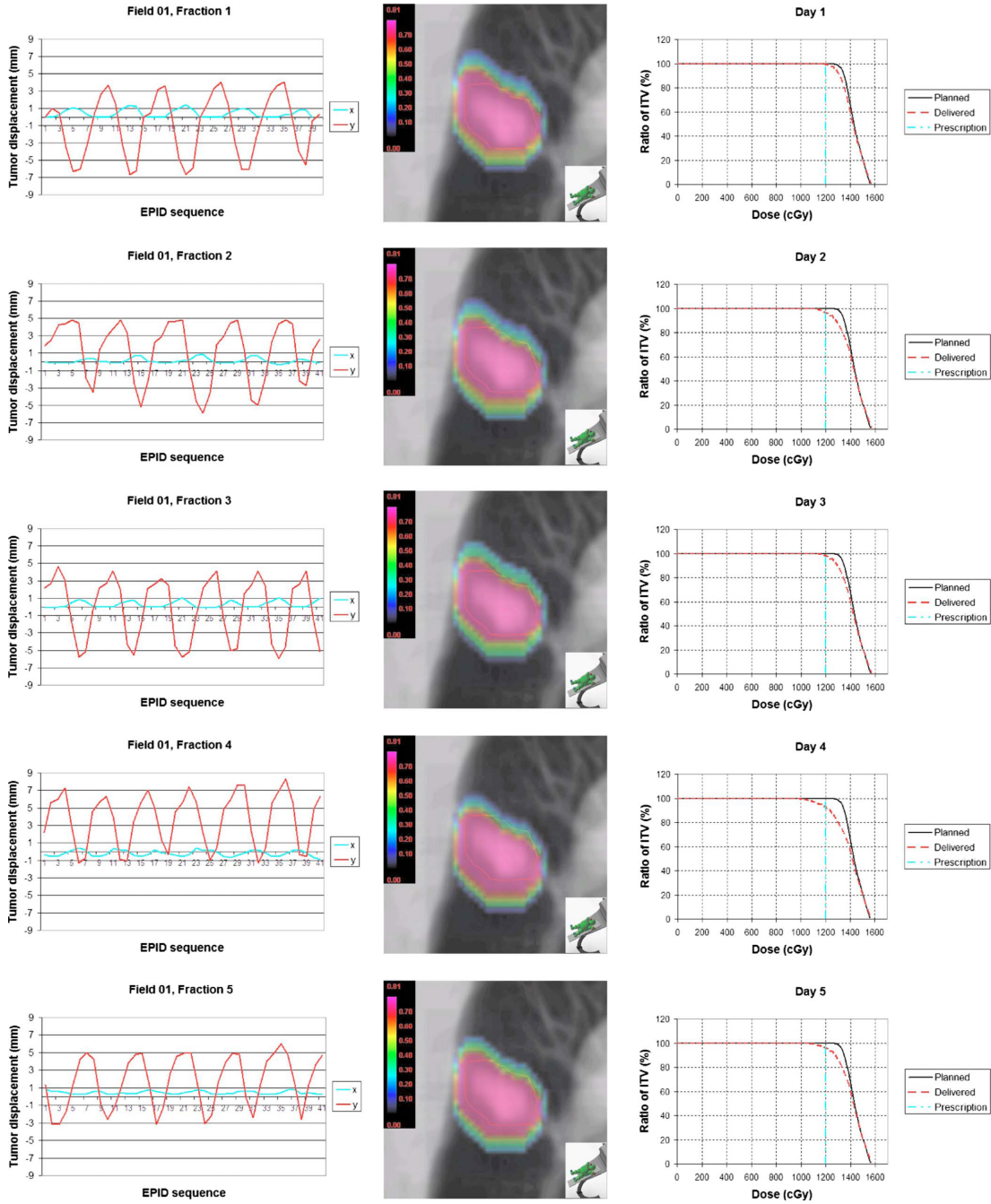
Figure 4.5: In the *(left)* column the tumor trajectories for the AP-Field (number 01) are shown for each treatment day as a showcase. The *(middle)* column shows the DRR field 01 for eeach fraction overlayed with a dose colorwash. In the *(right)* column the dose volume histograms (DVH) for the internal target volume (ITV) on each treatment day are given. The delivered dose appears to be generally lower than the planned. On day 4 and 5 the mean-shift indicates a large setup error, which manifests itself in a lower DVH for these days.
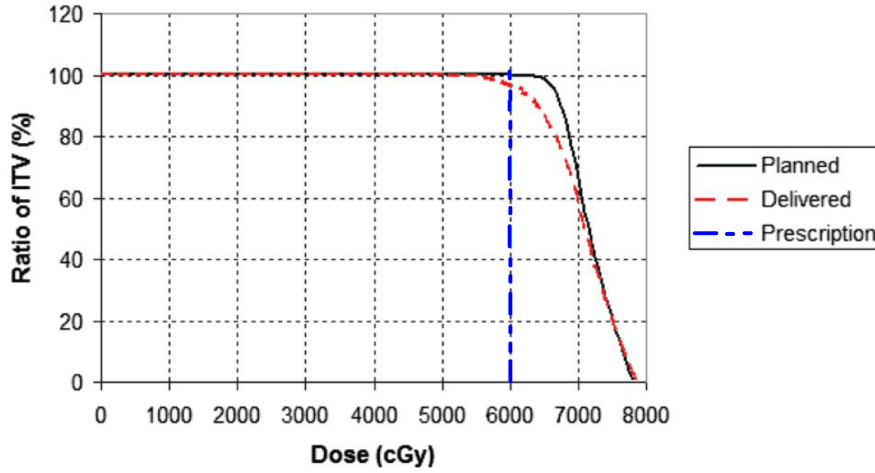
Figure 4.6: Dose Volume Histogram for the entire treatment course.

in fractions 4 and 5, in particular, the patient setup position appears to be offset from the planned position. Therefore, the ITV is not completely covered by the prescribed dose on theses treatment days. However, the the total delivered dose is close to the planned dose due to the better setup in the first three fractions (cp. DVH in Figure 4.6).

4.4   Summary and conclusions

The current clinical procedures for external beam radiation therapy rely entirely on the planning dose calculation. It is generally assumed that the dose actually delivered to the patient matches the planned dose despite obvious problems arising from the input data used for planning, e.g. limited motion range estimation from 4DCT (cp. James et al. [29]) and the challenging tasks of precise and reproducible patient setup on the treatment table (while the target moves due to respiration). Therefore the actual delivered dose to the patient may differ from the planned one. This is particularly significant for hypofractionated treatment protocols such as lung SBRT, delivering a complete course in only 3-5 fractions which increases the impact of each single fraction relative to a treatment course consisting of 30 fractions. To detect, investigate and potentially correct such problems, a fast and convenient way of delivered dose estimation has been developed and described in this chapter.

The STiL algorithm was employed to calculate the delivered dose for a patient's lung SBRT treatment, retrospectively. The procedure consists of 3 steps: in the first step the treatment delivery is monitored with continuous MV-EPID imaging. In the second step, the location of the tumor is estimated for each image, retrospectively, resulting in 2d tumor trajectories in the plane perpendicular to the beam direction (dosimetrically most relevant plane). In the third step, the fluence profiles used for dose calculation in the TPS are shifted according to the estimated tumor trajectory to simulate the tumor motion. The accumulated delivered fluence profile is then used in the TPS to calculate a delivered dose on the planning CT.

To perform the does calculation with currently available equipment within a reasonable computation time, some approximations had to be made:

(i) The patient in our model is assumed to be a rigid body, moving on the tumor trajectory observed during the treatment delivery. As already alluded to in the introduction to this chapter, respiration is a deformable process. In particular, the electron density will not stay constant in a particular voxel, thus influencing the deposited dose therein and in the surrounding voxels.

(ii) We sample the tumor motion at a relatively low frame rate (2 Hz) with respect to the observed breathing frequency of ≈ 0.2 Hz. This temporal resolution is (via the delivered fluence map approximation) carried through to the delivered dose calculation.

However, the strong advantage of the method investigated in this chapter is its simplicity and clinical availability: all tools utilized are currently available in the clinic; there is no risk to the patient arising from the method, nor do any treatment protocols have to be modified for the data acquisition. The delivered dose calculation can be done offline in time before the next fraction.
The accuracy of the dose calculation can be expected to improve further with the availability of real-time volumetric imaging and/or deformable registration techniques to account for the deformations expected from organ motion.

5 Summary and Conclusions

Context of this thesis

Cancer has been the second leading cause of death in the United States in 2011. Lung cancer is one of the deadliest types of cancer with a 5 year survival chance of only about 15%. While surgical resection has classically been the standard care for early stage non-small cell lung carcinomas (NSCLC) stereotactic body radiation therapy (SBRT) is now considered as an even sometimes favorable alternative treatment option. Compared to conventional radiotherapy with photons deliverd in about 30 treatment fractions, SBRT is delivered in only 3-5 fractions with a much higher fractional dose, steeper dose gradients and reduced safety margins to avoid excessive normal tissue toxicity.

Lung tumors can show large respiratory motion ranges limiting the treatment options with SBRT. Respiration induced lung tumor motion is most significant in the superior-inferior direction and shows hysteresis, i.e. inhale and exhale motion can be distinguished. The tumor motion range is factored into the treatment planning by assigning an internal target volume (ITV) which encloses all tumor positions observed during the image acquisition for treatment planning (usually 4DCT). The underlying assumption of the tumor motion during treatment delivery being similar to the motion observed for planning has been shown not to be always valid and may compromise the dose coverage or cause increased normal tissue toxicity. Additionally, setting up the patient on the treatment table to the moving lung tumor target can be challenging and introduce setup errors close to cm range.

Therefore, there is great demand for tools to monitor treatment setup and tumor motion during 3D conformal radiotherapy delivery accurately and in real-time.

Real-time lung tumor motion detection without implanted fiducial markers

The core to this thesis was the development of a method for markerless real-time lung tumor motion estimation that can be used during radiotherapy delivery with photons beams. The novelty of the approach presented in this thesis is that the algorithm utilizes the target area directly to estimate motion but at the same time does not require implanted fiducial markers as a tracking surrogate. This is a great advantage because it avoids the high risk of introducing a pneumothorax with the marker implantation procedure which could be potentially fatal for the patient.

The tumor motion is estimated from electronic portal images acquired with the treatment beam. The beams-eye-view imaging perspective of the electronic portal imaging device (EPID) brings the advantage of capturing both directions of the steep photon fluence falloff on the field edge. Thus, the dosimetrically most relevant motion information available from 2d projection images is captured (i.e. the plane perpendicular to the photon beam axis). Additionally taking MV-EPID images does not comprise any additional risk to the patient as for instance kV fluoroscopy imaging does with its imaging dose.

The motion estimation algorithm has been validated on both phantom data and patient data from lung SBRT treatments. For the verification on phantom data a realistic breathing dynamic thorax phantom was utilized. It featured a lung tumor insert manufactured by rapid prototyping from lung tumor contours of a patient's treatment planning CT. The phantom motion was directed in superior-inferior direction. A lung tumor motion trajectory recorded from a lung SBRT treatment delivery with the RTRT system in Hokkaido, Japan (utilizing implanted fiducial markers) was used to drive the phantom motion. The geometric accuracy of the tumor motion estimation was found to be better than $1\,mm$ throughout the experiment and the root mean square error was calculated to RMSE $= (0.8 \pm 0.2)\,mm$ in comparison to a reference trajectory created by manual registration.

Lung SBRT treatments were monitored with continuous MV-EPID imaging at a frame rate of 2 Hz. The tumor motion algorithm was validated on this data in a retrospective study: for the first 40 images of 56 beam-fractions tumor motion

trajectories were defined manually with the help of an interactive software tool developed for this purpose. Each image was presented 3 times in random order to the examiner in order to establish a reference tumor trajectory and a manual registration error. The manual registration error was taken to be the standard deviation of the 3 repetitions of each image and computed to RMSE $= (0.9 \pm 0.5) \, mm$. The geometric error of the motion estimation algorithm relative to this reference was found to be RMSE $= (2.1 \pm 1.7) \, mm$ while no tracking at all resulted in an error of RMSE $= (3.9 \pm 2.7) \, mm$.

The presented algorithm works with sub-millimeter accuracy on phantom data. For patient data the motion recovery performance is not as good as for phantom data yet significantly better than assuming a static target motion trajectory. The lower geometric accuracy on patient data arises mainly from the very low soft tissue contrast that can hardly be resembled with a tumor phantom.
The tracking accuracy depends mainly on the signal to noise ratio of the input images which is governed by the underlying physical properties of the detector as well as the object to be imaged. Lung tissue has a very low contrast for photons in the megavoltage range, so the contrast can generally be assumed to be rather weak.

While the method may not be quite ready for clinical application as an out of the box solution yet, future improvements in the detector design have the potential to vastly improve the accuracy and robustness of soft tissue localization with the algorithm.

Motion compensation through dynamic treatment aperture adaptation

As an application of the STiL algorithm a combined system integrating the algorithm with a dynamic multi-leaf collimator (DMLC) tracker has been built. The system allows to keep the treatment aperture fixated on the moving tumor during radiotherapy delivery. The system feeds MV-EPID images acquired with a (fast) frame grabbing device to the STiL algorithm, which estimates a tumor centroid position $p(t_i)$ in beams-eye-view coordinates. This position is fed to the DMLC control software, that calculates the shifted leaf positions accordingly and requests the new positions from the MLC hardware controller. The time needed from the point of acquisition of a new image to the MLC leafs reaching the requested target position (estimated from this image by the STiL algorithm)

is called system latency. Due to this system latency the treatment aperture position is lagging behind the tumor position introducing a systematic geometric error. In order to reduce this error a prediction algorithm was implemented. Linear (ridge) regression was chosen for its simplicity, speed and comparatively good results [36]. Operating the MV-EPID imaging device at a frame rate of 12.86 Hz (in half-resolution mode) the system latency was measured to $\delta t_s = 221 ms$. For this measurement the setup consisted of a resin phantom target moving with 20 mm superior-inferior motion range and 4.5 s cycle time on a translation stage made of solid water.

A simulation of the prediction algorithm based on the same lung tumor motion trajectories previously used to verify the the STiL algorithm showed that the geometric error with the use of the predictor decreases when compared to the error expected without prediction. Also, it was shown that the prediction model can be generated from external surrogate data as well.
The concept as a whole was physically validated with a dynamic phantom experiment using three of the trajectories previously employed for the simulation study. The geometric error between measured tumor position and aperture position showed that the system's dynamic treatment aperture can follow the tumor and reduce geometric errors: the error averaged over the three delivered trajectories was without any tracking calculated to RMSE $= (3\pm3.1)\, mm$. With tracking applied the error reduced to RMSE $= (0.7 \pm 0.7)\, mm$. Tracking without the use of the prediction algorithm resulted in an error of RMSE $= (1.7 \pm 1.7)\, mm$ on average for the three tumor trajectories investigated.

We have integrated the STiL algorithm with a DMLC tracking platform and characterized its performance. The system in its current state demonstrates the feasibility of DMLC tracking based on markerless soft tissue localization. We have shown that a motion error reduction can be achieved and that it can be further improved by implementing a simple (linear) prediction algorithm. In addition we have shown that external surrogate motion may be used to train the predictor model without significant loss of accuracy.
To make this system applicable to patients however, more research will have to be conducted to stabilize the STiL algorithm further and make the process of image acquisition more robust.

Delivered dose calculation

Tumor motion and setup uncertainties may have a significant impact on the delivered dose distribution. However, for lack of clinically available methods to calculate delivered dose for moving targets the planned dose has to be used instead as point of reference for treatment assessment and outcome studies.

We presented in this context a simple tool to monitor delivered dose based on 2D tumor trajectories calculated with the STiL algorithm. The procedure consists of 3 steps: in the first step the treatment delivery is monitored with continuous MV-EPID imaging; in the second one the location of the tumor is estimated for each image retrospectively resulting in 2d tumor trajectories in the plane perpendicular to the beam direction (dosimetrically most important plane). In the third step the fluence profiles used for dose calculation in the treatment planning system (TPS) are shifted according to the estimated tumor trajectory to simulate the tumor motion. The accumulated delivered fluence profile calculated in this fashion is imported back into the TPS to calculate a delivered dose on the planning CT.

We tested the procedure on the delivery of a lung SBRT treatment and calculated dose volume histograms to the ITV for each treatment fraction. The DVHs for the ITV showed that undercoverage occurs for large offsets from the mean tumor position during two out of five treatment days.
The advantages of the method include that it only uses tools already clinically available and the relatively fast calculation time. The latter point makes the method potentially suitable for delivered dose calculation in between treatment fractions in order to assess suspected errors and intervene with an adaptive therapy approach.

The simplicity of the dose calculation method comes at the price of accuracy: it has to be assumed that the patient's breathing motion can be approximated by a rigid body shift rather than a deformation process. However, considering that there is no alternative method currently available working with equipment already available in the clinic this is an excellent tool that allows to detect underdosage of the treatment volume as well as overdosage of the surrounding normal tissue.

Bibliography

[1] Cancer facts & figures 2011. American Cancer Society Inc., 250 Williams Street, NW, Atlanta, GA 30303-1002, 2011.

[2] L. E. Antonuk. Electronic portal imaging devices: a review and historical perspective of contemporary technologies and research. *Phys Med Biol*, 47 (6):R31–R65, Mar 2002.

[3] M. Aristophanous, J. Rottmann, L. E. Court, and R. I. Berbeco. Epid-guided 3d dose verification of lung sbrt. *Med Phys*, 38(1):495–503, Jan 2011.

[4] O. Belyaev, H. Herden, J. J. Meier, C. A. Muller, M. H. Seelig, T. Herzog, A. Tannapfel, W. E. Schmidt, and W. Uhl. Assessment of pancreatic hardness-surgeon versus durometer. *J Surg Res*, 158(1):53–60, Jan 2010. doi: 10.1016/j.jss.2008.08.022. URL http://dx.doi.org/10.1016/j.jss.2008.08.022.

[5] S. H. Benedict, K. M. Yenice, D. Followill, J. M. Galvin, W. Hinson, B. Kavanagh, P. Keall, M. Lovelock, S. Meeks, L. Papiez, T. Purdie, R. Sadagopan, M. C. Schell, B. Salter, D. J. Schlesinger, A. S. Shiu, T. Solberg, D. Y. Song, V. Stieber, R. Timmerman, W. A. Tomé, D. Verellen, L. Wang, and F.-F. Yin. Stereotactic body radiation therapy: the report of aapm task group 101. *Med Phys*, 37(8):4078–4101, Aug 2010.

[6] R. I. Berbeco, H. Mostafavi, G. C. Sharp, and S. B. Jiang. Towards fluoroscopic respiratory gating for lung tumours without radiopaque markers. *Phys Med Biol*, 50(19):4481–4490, Oct 2005. doi: 10.1088/0031-9155/50/19/004. URL http://dx.doi.org/10.1088/0031-9155/50/19/004.

[7] R. I. Berbeco, S. Nishioka, H. Shirato, G. T. Y. Chen, and S. B. Jiang. Residual motion of lung tumours in gated radiotherapy with external respiratory surrogates. *Phys Med Biol*, 50(16):3655–3667, Aug 2005. doi: 10.1088/

0031-9155/50/16/001. URL http://dx.doi.org/10.1088/0031-9155/50/16/001.

[8] H. Blomgren, I. Lax, I. Näslund, and R. Svanström. Stereotactic high dose fraction radiation therapy of extracranial tumors using an accelerator. clinical experience of the first thirty-one patients. *Acta Oncol*, 34(6):861–870, 1995.

[9] H. S. Bloom, E. L. Criswell, H. S. Pennypacker, A. C. Catania, and C. K. Adams. Major stimulus dimensions determining detection of simulated breast lesions. *Percept Psychophys*, 32(3):251–260, Sep 1982.

[10] J. Canny. A computational approach to edge detection. (6):679–698, 1986. doi: 10.1109/TPAMI.1986.4767851.

[11] Q. S. Chen, M. S. Weinhous, F. C. Deibel, J. P. Ciezki, and R. M. Macklis. Fluoroscopic study of tumor motion due to breathing: facilitating precise radiation therapy for lung cancer patients. *Med Phys*, 28(9):1850–1856, Sep 2001.

[12] L. E. Court, J. Seco, X.-Q. Lu, K. Ebe, C. Mayo, D. Ionascu, B. Winey, N. Giakoumakis, M. Aristophanous, R. Berbeco, J. Rottman, M. Bogdanov, D. Schofield, and T. Lingos. Use of a realistic breathing lung phantom to evaluate dose delivery errors. *Med Phys*, 37(11):5850–5857, Nov 2010.

[13] Y. Cui, J. G. Dy, B. Alexander, and S. B. Jiang. Fluoroscopic gating without implanted fiducial markers for lung cancer radiotherapy based on support vector machines. *Phys Med Biol*, 53(16):N315–N327, Aug 2008. doi: 10.1088/0031-9155/53/16/N01. URL http://dx.doi.org/10.1088/0031-9155/53/16/N01.

[14] W. D. D'Souza, S. A. Naqvi, and C. X. Yu. Real-time intra-fraction-motion tracking using the treatment couch: a feasibility study. *Phys Med Biol*, 50 (17):4021–4033, Sep 2005. doi: 10.1088/0031-9155/50/17/007. URL http://dx.doi.org/10.1088/0031-9155/50/17/007.

[15] L. Ekberg, O. Holmberg, L. Wittgren, G. Bjelkengren, and T. Landberg. What margins should be added to the clinical target volume in radiotherapy treatment planning for lung cancer? *Radiother Oncol*, 48(1):71–77, Jul 1998.

[16] F. Ernst and A. Schweikard. Forecasting respiratory motion with accurate online support vector regression (svrpred). *Int J Comput Assist Radiol Surg*, 4(5):439–447, Sep 2009. doi: 10.1007/s11548-009-0355-5. URL http://dx.doi.org/10.1007/s11548-009-0355-5.

[17] A. J. Fakiris, R. C. McGarry, C. T. Yiannoutsos, L. Papiez, M. Williams, M. A. Henderson, and R. Timmerman. Stereotactic body radiation therapy for early-stage non-small-cell lung carcinoma: four-year results of a prospective phase ii study. *Int J Radiat Oncol Biol Phys*, 75(3):677–682, Nov 2009. doi: 10.1016/j.ijrobp.2008.11.042. URL http://dx.doi.org/10.1016/j.ijrobp.2008.11.042.

[18] S. Flampouri, S. B. Jiang, G. C. Sharp, J. Wolfgang, A. A. Patel, and N. C. Choi. Estimation of the delivered patient dose in lung imrt treatment based on deformable registration of 4d-ct data and monte carlo simulations. *Phys Med Biol*, 51(11):2763–2779, Jun 2006. doi: 10.1088/0031-9155/51/11/006. URL http://dx.doi.org/10.1088/0031-9155/51/11/006.

[19] W. Fledelius, P. J. Keall, B. Cho, X. Yang, D. Morf, S. Scheib, and P. R. Poulsen. Tracking latency in image-based dynamic mlc tracking with direct image access. *Acta Oncol*, 50(6):952–959, Aug 2011. doi: 10.3109/0284186X.2011.581693. URL http://dx.doi.org/10.3109/0284186X.2011.581693.

[20] P. Giraud, S. Elles, S. Helfre, Y. De Rycke, V. Servois, M. F. Carette, C. Alzieu, P. Y. Bondiau, B. Dubray, E. Touboul, M. Housset, J. C. Rosenwald, and J. M. Cosset. Conformal radiotherapy for lung cancer: different delineation of the gross tumor volume (gtv) by radiologists and radiation oncologists. *Radiother Oncol*, 62(1):27–36, Jan 2002.

[21] I. S. Grills, V. S. Mangona, R. Welsh, G. Chmielewski, E. McInerney, S. Martin, J. Wloch, H. Ye, and L. L. Kestin. Outcomes after stereotactic lung radiotherapy or wedge resection for stage i non-small-cell lung cancer. *J Clin Oncol*, 28(6):928–935, Feb 2010. doi: 10.1200/JCO.2009.25.0928. URL http://dx.doi.org/10.1200/JCO.2009.25.0928.

[22] K. K. Herfarth, J. Debus, F. Lohr, M. L. Bahner, P. Fritz, A. Höss, W. Schlegel, and M. F. Wannenmacher. Extracranial stereotactic radiation therapy: set-up accuracy of patients treated for liver metastases. *Int J Radiat Oncol Biol Phys*, 46(2):329–335, Jan 2000.

[23] M. G. Herman, J. M. Balter, D. A. Jaffray, K. P. McGee, P. Munro, S. Shalev, M. Van Herk, and J. W. Wong. Clinical use of electronic portal imaging: report of aapm radiation therapy committee task group 58. *Med Phys*, 28 (5):712–737, May 2001.

[24] ICRU. Prescribing, recording and reporting photon beam therapy (icru report 50). Technical report, ICRU, 1993.

[25] ICRU. Prescribing, recording and reporting photon beam therapy (icru report 62, supplement to icru report no. 50). Technical report, ICRU, 1999.

[26] M. Imura, K. Yamazaki, H. Shirato, R. Onimaru, M. Fujino, S. Shimizu, T. Harada, S. Ogura, H. Dosaka-Akita, K. Miyasaka, and M. Nishimura. Insertion and fixation of fiducial markers for setup and tracking of lung tumors in radiotherapy. *International Journal of Radiation Oncology*Biology*Physics*, 63(5):1442 – 1447, 2005. ISSN 0360-3016. doi: 10.1016/j.ijrobp.2005.04.024. URL http://www.sciencedirect.com/science/article/pii/S0360301605007133.

[27] D. Ionascu, S. B. Jiang, S. Nishioka, H. Shirato, and R. I. Berbeco. Internal-external correlation investigations of respiratory induced motion of lung tumors. *Med Phys*, 34(10):3893–3903, Oct 2007.

[28] B. Jähne. *Digital Image Processing*. Springer-Verlag Berlin Heidelberg, 5th revised and extended edition edition, 2002.

[29] S. S. James, P. Mishra, F. Hacker, R. I. Berbeco, and J. H. Lewis. Quantifying itv instabilities arising from 4dct: a simulation study using patient data. *Phys Med Biol*, 57(5):L1–L7, Mar 2012. doi: 10.1088/0031-9155/57/5/L1. URL http://dx.doi.org/10.1088/0031-9155/57/5/L1.

[30] P. J. Keall, V. R. Kini, S. S. Vedam, and R. Mohan. Motion adaptive x-ray therapy: a feasibility study. *Phys Med Biol*, 46(1):1–10, Jan 2001.

[31] P. J. Keall, G. S. Mageras, J. M. Balter, R. S. Emery, K. M. Forster, S. B. Jiang, J. M. Kapatoes, D. A. Low, M. J. Murphy, B. R. Murray, C. R. Ramsey, M. B. V. Herk, S. S. Vedam, J. W. Wong, and E. Yorke. The management of respiratory motion in radiation oncology report of aapm task group 76. *Med Phys*, 33(10):3874–3900, Oct 2006.

[32] F. Khan. *The Physics of Radiation Therapy.* Lippincott Williams & Wilkins, 2009. ISBN 9780781788564. URL http://books.google.com/books?id=pWDQnxd-r1UC.

[33] W. Kilby and C. Savage. The effect of the varian amorphous silicon electronic portal imaging device on exit skin dose. *Phys Med Biol*, 48(19):3117–3128, Oct 2003.

[34] K. Kontrisova, M. Stock, K. Dieckmann, J. Bogner, R. Pötter, and D. Georg. Dosimetric comparison of stereotactic body radiotherapy in different respiration conditions: a modeling study. *Radiother Oncol*, 81(1):97–104, Oct 2006. doi: 10.1016/j.radonc.2006.08.006. URL http://dx.doi.org/10.1016/j.radonc.2006.08.006.

[35] N. Kothary, J. J. Heit, J. D. Louie, W. T. Kuo, B. W. Loo, A. Koong, D. T. Chang, D. Hovsepian, D. Y. Sze, and L. V. Hofmann. Safety and efficacy of percutaneous fiducial marker implantation for image-guided radiation therapy. *J Vasc Interv Radiol*, 20(2):235–239, Feb 2009. doi: 10.1016/j.jvir.2008.09.026. URL http://dx.doi.org/10.1016/j.jvir.2008.09.026.

[36] A. Krauss, S. Nill, and U. Oelfke. The comparative performance of four respiratory motion predictors for real-time tumour tracking. *Phys Med Biol*, 56(16):5303–5317, Aug 2011. doi: 10.1088/0031-9155/56/16/015. URL http://dx.doi.org/10.1088/0031-9155/56/16/015.

[37] P. A. Kupelian, A. Forbes, T. R. Willoughby, K. Wallace, R. R. Mañon, S. L. Meeks, L. Herrera, A. Johnston, and J. J. Herran. Implantation and stability of metallic fiducials within pulmonary lesions. *International Journal of Radiation Oncology*Biology*Physics*, 69(3):777 – 785, 2007. ISSN 0360-3016. doi: 10.1016/j.ijrobp.2007.03.040. URL http://www.sciencedirect.com/science/article/pii/S0360301607005548.

[38] J. P. Lewis. Fast template matching. In *Proc. Vision Interface 95, Canadian Image Processing and Pattern Recognition Society, Quebec City, CA*, pages 120–123, 15–19 May 1995.

[39] T. Lin, L. I. Cerviño, X. Tang, N. Vasconcelos, and S. B. Jiang. Fluoroscopic tumor tracking for image-guided lung cancer radiotherapy. *Phys Med Biol*, 54(4):981–992, Feb 2009. doi: 10.1088/0031-9155/54/4/011. URL http://dx.doi.org/10.1088/0031-9155/54/4/011.

[40] R. J. W. Louwe, E. M. F. Damen, M. van Herk, A. W. H. Minken, O. Torzsok, and B. J. Mijnheer. Three-dimensional dose reconstruction of breast cancer treatment using portal imaging. *Medical Physics*, 30(9):2376–2389, 2003. doi: 10.1118/1.1589496. URL http://link.aip.org/link/?MPH/30/2376/1.

[41] L. N. McDermott, M. Wendling, J. Nijkamp, A. Mans, J.-J. Sonke, B. J. Mijnheer, and M. van Herk. 3d in vivo dose verification of entire hypofractionated imrt treatments using an epid and cone-beam ct. *Radiotherapy and Oncology*, 86(1):35 – 42, 2008. ISSN 0167-8140. doi: 10.1016/j.radonc.2007.11.010. URL http://www.sciencedirect.com/science/article/pii/S0167814007005567.

[42] J. W. Motz and M. Danos. Image information content and patient exposure. *Med Phys*, 5(1):8–22, 1978.

[43] M. J. Murphy, J. Balter, S. Balter, J. A. BenComo, I. J. Das, S. B. Jiang, C. M. Ma, G. H. Olivera, R. F. Rodebaugh, K. J. Ruchala, H. Shirato, and F.-F. Yin. The management of imaging dose during image-guided radiotherapy: report of the aapm task group 75. *Med Phys*, 34(10):4041–4063, Oct 2007.

[44] B. Murray, K. Forster, and R. Timmerman. Frame-based immobilization and targeting for stereotactic body radiation therapy. *Med Dosim*, 32(2):86–91, 2007. doi: 10.1016/j.meddos.2007.01.005. URL http://dx.doi.org/10.1016/j.meddos.2007.01.005.

[45] S. M. J. J. G. Nijsten, B. J. Mijnheer, A. L. A. J. Dekker, P. Lambin, and A. W. H. Minken. Routine individualised patient dosimetry using electronic portal imaging devices. *Radiother Oncol*, 83(1):65–75, Apr 2007. doi: 10.1016/j.radonc.2007.03.003. URL http://dx.doi.org/10.1016/j.radonc.2007.03.003.

[46] M. Nikl. Scintillation detectors for x-rays. *Measurement Science and Technology*, 17(4):R37, 2006. URL http://stacks.iop.org/0957-0233/17/i=4/a=R01.

[47] S. Nill, J. Unkelbach, L. Dietrich, and U. Oelfke. Online correction for respiratory motion: evaluation of two different imaging geometries. *Phys*

Med Biol, 50(17):4087–4096, Sep 2005. doi: 10.1088/0031-9155/50/17/012. URL http://dx.doi.org/10.1088/0031-9155/50/17/012.

[48] P. R. Poulsen, B. Cho, A. Sawant, D. Ruan, and P. J. Keall. Detailed analysis of latencies in image-based dynamic mlc tracking. *Med Phys*, 37(9): 4998–5005, Sep 2010.

[49] R. Ramani, S. Russell, and P. O'Brien. Clinical dosimetry using mosfets. *Int J Radiat Oncol Biol Phys*, 37(4):959–64–, Mar. 1997. URL http://ukpmc. ac.uk/abstract/MED/9128975.

[50] D. Robinson. Inhomogeneity correction and the analytic anisotropic algorithm (aaa). *Journal of Applied Clinical Medical Physics*, 9(2), 2008. ISSN 15269914. URL http://www.jacmp.org/index.php/jacmp/article/ view/2786.

[51] P. Roesch, T. Mohs, T. Netsch, M. J. Quist, G. P. Penney, D. J. Hawkes, and J. Weese. Template selection and rejection for robust nonrigid 3d registration in the presence of large deformations. volume 4322, pages 545–556. SPIE, 2001. doi: 10.1117/12.431128. URL http://link.aip.org/link/?PSI/ 4322/545/1.

[52] J. Rottmann, M. Aristophanous, A. Chen, L. Court, and R. Berbeco. A multi-region algorithm for markerless beam's-eye view lung tumor tracking. *Phys Med Biol*, 55(18):5585–5598, Sep 2010. doi: 10.1088/0031-9155/55/ 18/021. URL http://dx.doi.org/10.1088/0031-9155/55/18/021.

[53] J. Rottmann, M. Aristophanous, A. Chen, L. Court, and R. Berbeco. Tu-e-204b-03: A multiregion algorithm for robust lung tumor tracking with portal image sequences. volume 37, pages 3401–3402. AAPM, 2010. doi: 10.1118/1.3469294. URL http://link.aip.org/link/?MPH/37/3401/4.

[54] J. Rottmann, M. Aristophanous, A. Chen, D. Sher, J. Killoran, F. Hacker, and R. Berbeco. Lung sbrt verification with continuous mv epid imaging, Nov. 2010. ISSN 0360-3016. URL http://linkinghub.elsevier.com/ retrieve/pii/S0360301610011132?showall=true.

[55] J. Rottmann, P. Keall, A. Chen, D. Sher, Y. Yue, and R. Berbeco. Dynamic treatment margin reduction for lung sbrt. volume 81, pages S769–S770.

Elsevier Science Inc., Oct. 2011. URL http://linkinghub.elsevier.com/retrieve/pii/S0360301611020086?showall=true.

[56] J. Rottmann, P. Keall, G. Cho, R. Hill, Y. Yue, and R. Berbeco. Tu-c-214-04: Prototype of a real-time adaptive therapy system integrating automatic soft tissue localization with dynamic multileaf collimator (dmlc) adaptation. volume 38, pages 3756–3757. AAPM, 2011. doi: 10.1118/1.3613136. URL http://link.aip.org/link/?MPH/38/3756/4.

[57] D. Ruan. Kernel density estimation-based real-time prediction for respiratory motion. *Phys Med Biol*, 55(5):1311–1326, Mar 2010. doi: 10.1088/0031-9155/55/5/004. URL http://dx.doi.org/10.1088/0031-9155/55/5/004.

[58] A. Sawant, R. Venkat, V. Srivastava, D. Carlson, S. Povzner, H. Cattell, and P. Keall. Management of three-dimensional intrafraction motion through real-time dmlc tracking. *Med Phys*, 35(5):2050–2061, May 2008.

[59] P. Scalchi and P. Francescon. Calibration of a mosfet detection system for 6-mv in vivo dosimetry. *International Journal of Radiation Oncology*Biology*Physics*, 40(4):987 – 993, 1998. ISSN 0360-3016. doi: 10.1016/S0360-3016(97)00894-8. URL http://www.sciencedirect.com/science/article/pii/S0360301697008948.

[60] Y. Seppenwoolde, H. Shirato, K. Kitamura, S. Shimizu, M. van Herk, J. V. Lebesque, and K. Miyasaka. Precise and real-time measurement of 3d tumor motion in lung due to breathing and heartbeat, measured during radiotherapy. *Int J Radiat Oncol Biol Phys*, 53(4):822–834, Jul 2002.

[61] G. C. Sharp, S. B. Jiang, S. Shimizu, and H. Shirato. Prediction of respiratory tumour motion for real-time image-guided radiotherapy. *Phys Med Biol*, 49(3):425–440, Feb 2004.

[62] H. Shirato, S. Shimizu, K. Kitamura, T. Nishioka, K. Kagei, S. Hashimoto, H. Aoyama, T. Kunieda, N. Shinohara, H. Dosaka-Akita, and K. Miyasaka. Four-dimensional treatment planning and fluoroscopic real-time tumor tracking radiotherapy for moving tumor. *Int J Radiat Oncol Biol Phys*, 48(2):435–442, Sep 2000.

[63] H. Shirato, M. Oita, K. Fujita, Y. Watanabe, and K. Miyasaka. Feasibility of synchronization of real-time tumor-tracking radiotherapy and intensity-modulated radiotherapy from viewpoint of excessive dose from fluoroscopy. *Int J Radiat Oncol Biol Phys*, 60(1):335–341, Sep 2004. doi: 10.1016/j.ijrobp. 2004.04.028. URL http://dx.doi.org/10.1016/j.ijrobp.2004.04.028.

[64] J.-J. Sonke and J. Belderbos. Adaptive radiotherapy for lung cancer. *Semin Radiat Oncol*, 20(2):94–106, Apr 2010. doi: 10.1016/j.semradonc.2009.11. 003. URL http://dx.doi.org/10.1016/j.semradonc.2009.11.003.

[65] Y. Suh, S. Dieterich, and P. J. Keall. Geometric uncertainty of 2d projection imaging in monitoring 3d tumor motion. *Phys Med Biol*, 52(12):3439–3454, Jun 2007. doi: 10.1088/0031-9155/52/12/008. URL http://dx.doi.org/ 10.1088/0031-9155/52/12/008.

[66] M. Tacke, S. Nill, and U. Oelfke. Real-time tracking of tumor motions and deformations along the leaf travel direction with the aid of a synchronized dynamic mlc leaf sequencer. *Phys Med Biol*, 52(22):N505–N512, Nov 2007. doi: 10.1088/0031-9155/52/22/N01. URL http://dx.doi.org/10.1088/ 0031-9155/52/22/N01.

[67] R. Timmerman, L. Papiez, R. McGarry, L. Likes, C. DesRosiers, S. Frost, and M. Williams. Extracranial stereotactic radioablation: results of a phase i study in medically inoperable stage i non-small cell lung cancer. *Chest*, 124 (5):1946–1955, Nov 2003.

[68] R. Timmerman, R. McGarry, C. Yiannoutsos, L. Papiez, K. Tudor, J. DeLuca, M. Ewing, R. Abdulrahman, C. DesRosiers, M. Williams, and J. Fletcher. Excessive toxicity when treating central tumors in a phase ii study of stereotactic body radiation therapy for medically inoperable early-stage lung cancer. *J Clin Oncol*, 24(30):4833–4839, Oct 2006. doi: 10.1200/JCO.2006.07.5937. URL http://dx.doi.org/10.1200/JCO.2006. 07.5937.

[69] J. Van de Steene, N. Linthout, J. de Mey, V. Vinh-Hung, C. Claassens, M. Noppen, A. Bel, and G. Storme. Definition of gross tumor volume in lung cancer: inter-observer variability. *Radiother Oncol*, 62(1):37–49, Jan 2002.

[70] J. P. Winston, K. Best, L. Plusquellic, P. Thoma, and D. G. Gilley. Patient exposure and dose guide - 2003. *CRCPD Publication E-03-2*, 2003.

[71] H. Wu, G. Sandison, L. Zhao, Q. Zhao, H. Shirato, and S. Jiang. Correlation between parameters describing tumour motion and its location in the lungs. *Australas Phys Eng Sci Med*, 30(4):341–344, Dec 2007.

[72] J. Wulf, U. Hädinger, U. Oppitz, W. Thiele, R. Ness-Dourdoumas, and M. Flentje. Stereotactic radiotherapy of targets in the lung and liver. *Strahlenther Onkol*, 177(12):645–655, Dec 2001.

[73] Q. Xu, R. J. Hamilton, R. A. Schowengerdt, and S. B. Jiang. A deformable lung tumor tracking method in fluoroscopic video using active shape models: a feasibility study. *Phys Med Biol*, 52(17):5277–5293, Sep 2007. doi: 10.1088/0031-9155/52/17/012. URL http://dx.doi.org/10.1088/0031-9155/52/17/012.

[74] D. Yan, F. Vicini, J. Wong, and A. Martinez. Adaptive radiation therapy. *Phys Med Biol*, 42(1):123–132, Jan 1997.

Acknowledgements